Monthly Notices
of the
ROYAL ASTRONOMICAL SOCIETY

MNRAS **478,** 2737–2752 (2018)
Advance Access publication 2018 May 4

doi:10.1093/mnras/sty1166

Dusty disc–planet interaction with dust-free simulations

Jhih-Wei Chen[1,2] and Min-Kai Lin[1]★

[1]*Institute of Astronomy and Astrophysics, Academia Sinica, Taipei 10617, Taiwan*
[2]*Department of Electrical Engineering, National Taiwan University, Taipei 10617, Taiwan*

Accepted 2018 May 1. Received 2018 May 1; in original form 2018 March 21

ABSTRACT

Protoplanets may be born into dust-rich environments if planetesimals formed through streaming or gravitational instabilities, or if the protoplanetary disc is undergoing mass-loss due to disc winds or photoevaporation. Motivated by this possibility, we explore the interaction between low-mass planets and dusty protoplanetary discs with focus on disc–planet torques. We implement Lin & Youdin's newly developed, purely hydrodynamic model of dusty gas into the PLUTO code to simulate dusty protoplanetary discs with an embedded planet. We find that for imperfectly coupled dust and high metallicity, e.g. Stokes number 10^{-3} and dust-to-gas ratio $\Sigma_{\rm d}/\Sigma_{\rm g} = 0.5$, a 'bubble' develops inside the planet's co-orbital region, which introduces unsteadiness in the flow. The resulting disc–planet torques sustain large amplitude oscillations that persists well beyond that in simulations with perfectly coupled dust or low dust-loading, where co-rotation torques are always damped. We show that the desaturation of the co-rotation torques by finite-sized particles is related to potential vorticity generation from the misalignment of dust and gas densities. We briefly discuss possible implications for the orbital evolution of protoplanets in dust-rich discs. We also demonstrate Lin & Youdin's dust-free framework reproduces previous results pertaining to dusty protoplanetary discs, including dust-trapping by pressure bumps, dust-settling, and the streaming instability.

Key words: accretion, accretion discs – hydrodynamics – methods: numerical – planet-disc interactions – protoplanetary discs.

1 INTRODUCTION

The gravitational interaction between protoplanets and their protoplanetary disc, which leads to the planet's orbital evolution, likely plays a key role in shaping the architecture of planetary systems (Baruteau et al. 2014, 2016). It is thus necessary to understand how realistic disc conditions affect planet–disc interaction.

Since the pioneering study of Goldreich & Tremaine (1980) almost four decades ago, the disc–planet problem has been extended to include many physical effects expected in protoplanetary discs. These include turbulence (e.g. Nelson & Papaloizou 2003; Baruteau, Fromang, Nelson & Masset 2011b; Uribe et al. 2011; Stoll, Picogna & Kley 2017) or lack thereof (e.g. Rafikov 2002; Li et al. 2009; Fung & Chiang 2017); large-scale magnetic fields (e.g. Terquem 2003; Guilet, Baruteau & Papaloizou 2013; McNally et al. 2017); dynamical torques (e.g. Masset & Papaloizou 2003; Pepliński, Artymowicz & Mellema 2008; Paardekooper 2014); disc self-gravity (e.g. Baruteau & Masset 2008b; Zhang et al. 2008; Baruteau et al. 2011a); planet-induced instabilities (e.g. Koller, Li & Lin 2003; Li et al. 2005; Lin & Papaloizou 2011; Fu et al. 2014a); and non-isothermal discs (e.g. Paardekooper & Mellema 2006, 2008; Baruteau & Masset 2008a; Masset & Casoli 2010; Paardekooper et al. 2010; Benítez-Llambay et al. 2015), to name a few. While these studies present important generalizations, they have been limited to purely gaseous discs.

However, protoplanetary discs are dusty (Testi et al. 2014). It is thus natural to consider dusty disc–planet interaction (e.g. Paardekooper & Mellema 2004; Fouchet et al. 2007; Ayliffe et al. 2012; Zhu et al. 2012; Dipierro et al. 2016; Dipierro & Laibe 2017). Recent efforts in this direction have been largely motivated by observations of dusty sub-structures in protoplanetary discs (e.g. van der Marel et al. 2013; ALMA Partnership 2015; Andrews et al. 2016; Cieza et al. 2017; van Boekel et al. 2017; van der Plas et al. 2017); as disc–planet interaction is a potential mechanism to generate dust rings (Dipierro et al. 2015; Picogna & Kley 2015; Jin et al. 2016; Rosotti et al. 2016; Bae, Zhu & Hartmann 2017; Dong et al. 2017) and dust clumps (Lyra et al. 2009; Fu et al. 2014b; Zhu et al. 2014; Bae, Zhu & Hartmann 2016) observed in these systems. These studies thus focus on the dust morphology instead of the planet's response to the dusty disc. For a typical dust-to-gas ratio of $\sim$1 per cent, one may not expect disc-planet torques to differ from pure gas models. Recently, however, Benítez-Llambay & Pessah (2018) performed the first study on the effect of dust dynamics on

★ E-mail: mklin@asiaa.sinica.edu.tw

planetary torques, and found that dust cannot be ignored even at such low metallicities.

On the other hand, planet migration in discs with high dust-to-gas ratios has not been studied in detail. This, however, appears to be a natural limit to consider, since planetesimal formation in the first place may require dust-rich environments (Johansen et al. 2014). Examples include gravitational instability (Goldreich & Ward 1973) and the streaming instability, which typically require local dust-to-gas ratios >1 to operate efficiently (Youdin & Goodman 2005; Johansen & Youdin 2007). Several processes can enhance the dust-to-gas ratio, including vertical dust-settling (Takeuchi & Lin 2002); gas mass-loss due to photoevaporation (Alexander et al. 2014) or magnetic winds (Bai 2016); and feedback of dust-drag on the gas (Gonzalez, Laibe & Maddison 2017; Kanagawa et al. 2017).

Motivated by these considerations, we explore the interaction between dust-rich discs and embedded planets with focus on disc–planet torques. In order to connect with previous studies of planet migration in pure gas discs, it is desirable to model dusty gas as a single fluid. Such an approach was recently presented by Laibe & Price (2014) and Price & Laibe (2015), and further developed by Lin & Youdin (2017, hereafter LY17).

LY17 showed that for sufficiently small dust particles mixed with polytropic gas, the dusty-gas system is equivalent to pure-gas dynamics subject to cooling/heating. Since gaseous disc–planet interaction has been well studied, this connection allows us to understand new results obtained from dusty discs in terms of established results based on pure gas discs. This work presents the first numerical application of LY17's framework.

This paper is organized as follows. In Section 2, we first review LY17's dust-free description of dusty protoplanetary discs and its numerical implementation. In Section 3, we describe equilibrium 2D disc models. In Section 4, we present numerical simulations of low-mass planets embedded in 2D dusty discs with emphasis on disc–planet torques. We find for sufficiently large particles and dust-loading, that disc–planet torques remain oscillatory for extended periods of time compared to small particles and/or dust-to-gas ratios. We summarize and discuss potential implications of these results in Section 5. In the Appendices, we present additional simulations to demonstrate LY17's framework reproduces several standard results in 2D and 3D dusty discs, including dust-trapping at planet gaps, the streaming instability, and dust-settling.

2 DUST-FREE MODELLING OF DUSTY PROTOPLANETARY DISCS

In this section, we review the dust-free description of dusty protoplanetary discs developed by LY17. This is achieved by assuming small dust particles and polytropic gas. The governing equations for dusty gas discs can then be written in a form similar to pure gas dynamics and readily implemented into existing hydrodynamic codes.

The physical system of interest is a dusty accretion disc orbiting a central star of mass M_*. Disc self-gravity, magnetic fields, and viscosity are neglected. Cylindrical (R, φ, z) and spherical (r, θ, φ) coordinates are centred on the star. The gas phase has density, pressure, and velocity fields ρ_g, P, $\boldsymbol{v}_g$, respectively. The disc is nearly Keplerian with angular velocity $\Omega \simeq \Omega_K(R) \equiv \sqrt{GM_*/R^3}$ where G is the gravitational constant.

2.1 Simplifying assumptions

We consider small dust particles strongly but not necessarily perfectly coupled to the gas. We approximate the dust particles as a single, pressureless fluid with density ρ_d and velocity $\boldsymbol{v}_d$ (Jacquet, Balbus & Latter 2011). The mutual dust–gas drag is characterized by the stopping time t_s such that

$$\rho_d \left.\frac{\partial \boldsymbol{v}_d}{\partial t}\right|_{drag} = -\rho_g \left.\frac{\partial \boldsymbol{v}_g}{\partial t}\right|_{drag} = -\frac{\rho_g \rho_d}{\rho}\frac{(\boldsymbol{v}_d - \boldsymbol{v}_g)}{t_s}. \quad (1)$$

is the dust–gas friction force per unit volume, where

$$\rho \equiv \rho_g + \rho_d \quad (2)$$

is the total density.

We consider the Epstein regime with relative stopping times given by $t_s = \rho_\bullet s_\bullet / \rho c_s$ (Weidenschilling 1977), where $\rho_\bullet$, $s_\bullet$ is the internal density and radius of a grain, respectively; and c_s is the gas sound-speed (see below). In practice, we specify the dimensionless stopping time or Stokes number T_{stop} such that

$$t_s = \frac{\rho_0 c_{s0}}{\rho c_s}\frac{T_{stop}}{\Omega_{K0}}, \quad (3)$$

where subscript 0 here and below corresponds to evaluation at the reference cylindrical radius R_0 and disc mid-plane $z = 0$. Note that our definition of the stopping time is related to the particle stopping time $\tau_s = t_s \rho / \rho_g$.

2.1.1 Terminal velocity approximation

We assume the particles are sufficiently small so their stopping times satisfy

$$t_s \Omega_K \ll 1. \quad (4)$$

In this limit the dust velocity $\boldsymbol{v}_d$ can be obtained from the *terminal velocity approximation*:

$$\boldsymbol{v}_d = \boldsymbol{v}_g + t_s \frac{\nabla P}{\rho_g} \quad (5)$$

(Youdin & Goodman 2005; Jacquet et al. 2011; Price & Laibe 2015, LY17). Equation (5) is a key approximation in our model. It reflects the fact that particles tend to drift towards pressure maxima (Whipple 1972; Weidenschilling 1977).

2.1.2 Polytropic gas

The second simplification we make is to consider polytropic gas, where the thermal pressure P is given by

$$P = c_s^2(R)\rho_{g0}\left(\frac{\rho_g}{\rho_{g0}}\right)^\xi \equiv K(R)\rho_g^\xi, \quad (6)$$

where $c_s(R)$ is prescribed below and ξ is the constant polytropic index. In practice we consider $\xi \simeq 1$ or isothermal gas. Equation (6) is to hold at all times. For an ideal gas the disc temperature T can be obtained from $P = \mathcal{R}\rho_g T$, where $\mathcal{R}$ is the gas constant, so $c_s^2 \propto T$ for $\xi = 1$.

We take vertically isothermal, power-law radial temperature profiles so that,

$$c_s^2(R) = c_{s0}^2\left(\frac{R}{R_0}\right)^{-q}. \quad (7)$$

We also define

$$H_{\rm g}(R) \equiv \frac{c_s(R)}{\Omega_{\rm K}(R)}. \tag{8}$$

This is the pressure scale height for a vertically isothermal, pure gas disc. The corresponding aspect-ratio is $h_{\rm g} \equiv H_{\rm g}/R$.

By adopting the terminal velocity approximation, we eliminate the need to solve for the dust velocity $\boldsymbol{v}_{\rm d}$; and by adopting a polytropic gas we eliminate the need for a gas energy equation. However, we show below that the mixture still obeys an effective energy equation, which completes the analogy with hydrodynamics.

2.2 Governing equations

With the above approximations the dusty accretion disc can be described (in a rotating frame with angular velocity $\Omega_{\rm K0}\hat{\boldsymbol{z}}$) by

$$\frac{D\rho}{Dt} = -\rho\nabla\cdot\boldsymbol{v}, \tag{9}$$

$$\frac{D\boldsymbol{v}}{Dt} = -\tfrac{1}{\rho}\nabla P - \nabla\Phi - 2\Omega_{\rm K0}\hat{\boldsymbol{z}}\times\boldsymbol{v}, \tag{10}$$

$$\frac{Df_{\rm d}}{Dt} = -\tfrac{1}{\rho}\nabla\cdot(f_{\rm d}t_{\rm s}\nabla P) \tag{11}$$

(LY17), where $\boldsymbol{v} = \left(\rho_{\rm d}\boldsymbol{v}_{\rm d} + \rho_{\rm g}\boldsymbol{v}_{\rm g}\right)/\rho$ is the mixture's centre of mass velocity; Φ is an effective gravitational potential; and the dust-fraction $f_{\rm d} = \rho_{\rm d}/\rho$ is also given via the dust-to-gas ratio $\epsilon = \rho_{\rm d}/\rho_{\rm g} = f_{\rm d}/(1-f_{\rm d})$.

Equations (9) and (10) describe the conservation of total mass and momentum of the mixture, respectively. Equation (11) results from dust mass conservation with the terminal velocity approximation. The diffusion-like term on the right-hand side of equation (11) accounts for the effect of finite dust–gas coupling. If $t_{\rm s} = 0$ then dust is perfectly coupled to the gas, and $f_{\rm d}$ is advectively conserved. When $t_{\rm s} > 0$, dust can slip past the gas and drift towards pressure maxima.

We refer the reader to Laibe & Price (2014) for a derivation of these equations in the non-rotating frame and Price & Laibe (2015) for an implementation in smoothed particle hydrodynamics. Recent applications can be found in Ragusa et al. (2017) and Tricco, Price & Laibe (2017). We will implement an alternate form of these equations in grid-based hydrodynamics.

2.3 Gravitational potential

In the rotating frame the total gravitational potential is

$$\Phi(R,\phi,z) = \Phi_*(R,z) + \Phi_p(R,\phi,z) - \tfrac{1}{2}R^2\Omega_{\rm K0}^2. \tag{12}$$

Here,

$$\Phi_*(R,z) = -\frac{GM_*}{\sqrt{R^2+z^2}} \simeq -R^2\Omega_{\rm K}^2\left(1-\frac{z^2}{2R^2}\right). \tag{13}$$

is the stellar potential, and the second equality is its approximate form in a thin-disc ($|z| \ll R$)

We also allow for a planet fixed on a Keplerian circular orbit at radius R_0 at the disc mid-plane. Placing the planet at $\varphi = \pi$ in the rotating frame, the planet potential is

$$\Phi_p(R,\phi,z) = -\frac{GM_p}{\sqrt{R^2+R_0^2-2RR_0\cos(\phi-\pi)+z^2+r_s^2}} + \frac{GM_p}{R_0^2}R\cos(\phi-\pi), \tag{14}$$

where r_s is the softening length. The second term is the indirect potential to account for the acceleration of the star–planet system centre of mass.

2.4 Dust evolution as effective energy equations

Equation (11), which governs dust evolution, may be recast into a more familiar form by noting the dust-fraction can be eliminated from the problem by using the gas equation of state, equation (6):

$$f_{\rm d} = 1 - \frac{1}{\rho}\left(\frac{P}{K}\right)^{1/\xi}. \tag{15}$$

Then equation (11) can be converted to read

$$\frac{{\rm D}P}{{\rm D}t} = -\xi P\nabla\cdot\boldsymbol{v} + P\boldsymbol{v}\cdot\nabla\ln c_s^2 + \frac{\xi P}{\rho_{\rm g}}\nabla\cdot(f_{\rm d}t_{\rm s}\nabla P), \tag{16}$$

with $\rho_{\rm g} = \rho_{\rm g}(P;R)$ from equation (6) and $f_{\rm d} = f_{\rm d}(P,\rho;R)$ from equation (15).

Notice equation (16) is identical in form to the pressure equation of a pure, ideal gas with adiabatic index $\gamma = \xi$, subject to heating and cooling. However, equation (16) does not physically reflect the mixture's energy, but is just a consequence of assuming a polytropic gas together with dust mass conservation and the terminal velocity approximation (LY17). Nevertheless, we use equation (16) instead equation (11) to convert the dusty problem to standard hydrodynamics. Equations (9), (10), and (16) are three equations for the unknowns (ρ, $\boldsymbol{v}$, P). Although the physical system describes dusty gas, dust does not make an explicit appearance in the equations: the model is pure hydrodynamical.

The main advantage of evolving the pressure via equation (16) instead of using equation (6) is practical ease in the numerical implementation of dust evolution, equation (11) (see Section 2.6). Furthermore, modelling the dusty problem in a dust-free manner allows us to generalize pure gas phenomena to dusty discs and gain physical insight. Our dust-free model connects our new results on dusty disc–planet torques to previous results established for pure gas discs (e.g. Paardekooper et al. 2010).

In the Appendices, we demonstrate this hydrodynamic framework reproduces several other expected results related to dust–gas interaction in protoplanetary discs. These include radial dust drift and dust-trapping at planet gaps (Appendix A); the streaming instability (Appendix B); and dust-settling (Appendix C). The latter two cases consider 3D discs.

2.4.1 Effective total energy

If we define the effective total energy density E with

$$E \equiv \frac{P}{\xi-1} + \frac{1}{2}\rho|\boldsymbol{v}|^2 + \rho\Phi, \tag{17}$$

then combining equations (10) and (16) gives

$$\frac{\partial E}{\partial t} + \nabla\cdot[(E+P)\boldsymbol{v}] = \frac{P}{\xi-1}\boldsymbol{v}\cdot\nabla\ln c_s^2 + \frac{\xi P}{\rho_{\rm g}(\xi-1)}\nabla\cdot(f_{\rm d}t_{\rm s}\nabla P), \tag{18}$$

where we have assumed a time-independent gravitational potential, so $\partial_t\Phi = 0$.

It should be emphasized that E does not represent the true total energy density of the dusty gas. Instead, E is simply defined such that upon combining the momentum and mass conservation equations with the polytropic equation of state (equation 6), we arrive at an

evolutionary equation (18) that is similar in form to the total energy equation of a pure gas with source terms. The first term on the right-hand-side (RHS) is analogous to optically thin cooling: it reflects the fixed temperature profile imposed upon the system (equation 7). The second, diffusion-like term reflects particle drift relative to the gas.

2.4.2 *Effective entropy*

We can also recast the thermal energy evolution (equation 16) in terms of entropy evolution by defining the mixture's effective (dimensionless) entropy as $S = \ln(P/\rho^{\xi})$. Then

$$\frac{\mathrm{D}S}{\mathrm{D}t} = \boldsymbol{v}\cdot\nabla\ln c_s^2 + \frac{\xi}{\rho_\mathrm{g}}\nabla\cdot(f_\mathrm{d}t_\mathrm{s}\nabla P)\,. \tag{19}$$

This form is appropriate for hydrodynamic codes that evolve the system entropy, rather than energy.

2.4.3 *Physical interpretation*

Although the true disc temperature T is prescribed via the equation of state (equation 7), the dusty-gas mixture still obeys an effective energy equation, converted from the dust evolutionary equation. This indicates that the mixture possesses a 'dynamic' temperature $\widetilde{T}$ that depends on the dust-to-gas ratio.

To see this, let us regard the mixture as a single ideal fluid with $P = \mathcal{R}\rho\widetilde{T}$. As the pressure is actually given by $P = \mathcal{R}\rho_\mathrm{g}T$, we find

$$\widetilde{T} = \frac{T}{1+\epsilon}, \tag{20}$$

and recall $\epsilon = \rho_\mathrm{d}/\rho_\mathrm{g}$. Thus, increasing the dust-to-gas ratio lowers the mixture's dynamic temperature. This occurs because dust-loading increases the mixture's inertia, but it does not contribute to thermal pressure.

The above discussion implies the effective sound speed ($\simeq\sqrt{P/\rho}$) of a dusty disc is reduced by a factor of $\sqrt{1+\epsilon}$. Thus, the effective scale height $\widetilde{H}$ is also reduced:

$$\widetilde{H} = \frac{H_\mathrm{g}}{\sqrt{1+\epsilon}}, \tag{21}$$

and we can define the effective aspect-ratio $\widetilde{h} \equiv \widetilde{H}/R$. The disc becomes thinner with increasing dust-load at fixed (true) temperature.

In LY17's model, dust-loading is interpreted as reducing the dynamic temperature or sound-speed, so a positive particle flux is analogous to a negative heat flux. A particle drift towards a pressure maximum constitutes to cooling the location of the maximum. This explains why dust–gas drag appears in an effective energy equation instead of the momentum equation.

2.5 Potential vorticity generation

It is important to notice that the dusty gas mixture is *baroclinic*, because the pressure arises solely from the gas, while the total density involves both gas and dust. This means the potential vorticity (PV) or vortensity is generally not conserved, because dust and gas need not be aligned if they can drift relative to each other.

The PV in the inertial frame is

$$\boldsymbol{\zeta} \equiv \frac{\nabla\times\boldsymbol{v} + 2\Omega_\mathrm{K0}\hat{\boldsymbol{z}}}{\rho}. \tag{22}$$

It obeys

$$\frac{\mathrm{D}\boldsymbol{\zeta}}{\mathrm{D}t} = \boldsymbol{\zeta}\cdot\nabla\boldsymbol{v} + \frac{1}{\rho^3}\nabla\rho\times\nabla P. \tag{23}$$

The second, baroclinic source term, is generally non-zero. For our equation of state $P \propto c_s^2(R)\rho_\mathrm{g}^{\xi}$ (equation 6) we find

$$\nabla\rho\times\nabla P = P\nabla\rho\times\nabla\ln c_s^2 + \frac{\xi P}{\rho_\mathrm{g}}\nabla\rho_\mathrm{d}\times\nabla\rho_\mathrm{g}. \tag{24}$$

The first term reflects baroclinity due misalignment between the (imposed) temperature profile and the total density. In the 2D, razor-thin discs models we consider later, this misalignment requires $\partial_R c_s^2 \neq 0$ with a non-axisymmetric total density distribution, $\partial_\phi\rho \neq 0$. However, this source of baroclinity is negligible in our disc–planet models.

Baroclinity may also arise from a misalignment between gas and dust densities, $\nabla\rho_\mathrm{d}\times\nabla\rho_\mathrm{g} \neq 0$, which requires a non-uniform dust-to-gas ratio. For our disc models below this non-uniformity – and hence baroclinity – largely develops from finite dust–gas drag (equation 11).

The baroclinic nature of dusty gas was already pointed out by Laibe & Price (2014). In this work, we present a realization of this effect in disc–planet interaction. Namely, we will show that PV can be generated from dust–gas misalignment near the planet due to dust–gas drift.

2.6 Numerical implementation

Fortunately, many publicly available hydrodynamic codes solve the energy equation in the form of equation (18). In this work, we use PLUTO[1] (Mignone et al. 2007, 2012) – a general purpose, finite-volume Godunov code for simulating astrophysical fluids. It can treat a variety of non-ideal hydrodynamic effects, including energy source terms similar to the RHS of equation (18). Thus, little effort is needed to convert PLUTO into a dusty hydrodynamics code.

The true disc temperature profile is imposed by the ∇c_s^2 term on the RHS of equation (18). For this we enable PLUTO's optically thin cooling module to update the pressure by solving

$$\frac{\partial P}{\partial t} = Pv_R\partial_R\ln c_s^2, \quad\Rightarrow\quad \Delta P = P\left[\exp\left(-q\frac{v_R}{R}\Delta t\right)-1\right], \tag{25}$$

where ΔP and Δt is the pressure update and time-step, respectively; and we have used equation (7).

Dust–gas drag is represented by second, diffusive term on the RHS of equation (18). For this we enable PLUTO's thermal conduction module. The original module updates the total energy E by solving

$$\frac{\partial E}{\partial t} = \nabla\cdot(\kappa_\mathrm{T}\nabla T), \tag{26}$$

where $T \propto P/\rho$ is the temperature field and κ_T is the thermal conduction coefficient. We adapt the module by replacing the temperature gradient in equation (26) with the pressure gradient,

$$\nabla T \to \nabla P, \tag{27}$$

and setting the thermal conduction coefficient to

$$\kappa_\mathrm{T} \to f_\mathrm{d}t_\mathrm{s}, \tag{28}$$

with $f_\mathrm{d} = f_\mathrm{d}(\rho, P; R)$ via equation (15). Finally, we scale the thermal conduction term by $\xi P/\rho_\mathrm{g}(\xi - 1)$, see equation (18). In practice this scaling factor is almost a constant because we choose $\xi \simeq 1$.

[1] http://plutocode.ph.unito.it

We use PLUTO's Super-Time-Stepping algorithm to integrate the dust diffusion term.

3 RAZOR-THIN DISCS

In this paper, we mostly consider 2D, razor-thin discs. To obtain the 2D disc equations from the full 3D models above, we replace ρ by the surface density Σ (similarly for the dust and gas components) and re-interpret P as the vertically integrated pressure. Thus, for example, the equation of state becomes $P = K\Sigma_{\rm g}^{\xi}$. We set $v_z = 0$ and the potential functions in Section 2.3 are evaluated at $z = 0$. Alternatively, we can consider these 2D models to represent a layer of disc material about the disc mid-plane.

3.1 Equilibrium structure

We initialize the 2D disc in an axisymmetric, steady state with total surface density $\Sigma = \Sigma(R) = \Sigma_{\rm g}[1 + \epsilon(R)]$ and velocity field $v_\varphi(R) = R[\Omega(R) - \Omega_{\rm K0}]$, $v_R = 0$. These satisfy the equilibrium radial momentum and energy equations (without a planet)

$$R\Omega^2 = R\Omega_{\rm K}^2(R) + \frac{1}{\Sigma}\frac{{\rm d}P}{{\rm d}R}, \tag{29}$$

$$0 = \frac{\rm d}{{\rm d}R}\left(Rf_{\rm d}t_{\rm s}\frac{{\rm d}P}{{\rm d}R}\right). \tag{30}$$

We set the initial gas surface density to

$$\Sigma_{\rm g}(R) = \Sigma_{\rm g0}\left(\frac{R}{R_0}\right)^{-p}. \tag{31}$$

For a non-self-gravitating problem, the surface density scale $\Sigma_{\rm g0}$ is arbitrary.

To obtain Σ from $\Sigma_{\rm g}$ we choose $\epsilon(R)$ to satisfy 'thermal' equilibrium, equation (30). This equation implies

$$\frac{\epsilon}{(1+\epsilon)^2}c_s(R)\Sigma_{\rm g}^{\xi-1}(R) \times \frac{{\rm d}\ln P}{{\rm d}\ln R} = \text{constant}, \tag{32}$$

where we have used the 2D version of the Epstein drag law, equation (3). For power-law discs with generally non-zero pressure gradients, we require the first factor to be constant. We thus obtain $\epsilon(R)$ from

$$\frac{\epsilon(R)}{[1+\epsilon(R)]^2} = \frac{\epsilon_0}{(1+\epsilon_0)^2}\left[\frac{c_{s0}}{c_s(R)}\right]\left[\frac{\Sigma_{\rm g0}}{\Sigma_{\rm g}(R)}\right]^{\xi-1} \equiv F(R).$$

Notice

$$\frac{(1-\epsilon)}{(1+\epsilon)^3}\frac{{\rm d}\epsilon}{{\rm d}R} = \frac{{\rm d}F}{{\rm d}R}. \tag{33}$$

For typical disc models ${\rm d}F/{\rm d}R > 0$. Then dust-poor discs ($\epsilon < 1$) have dust-to-gas ratios increasing with R; whereas dust-rich discs ($\epsilon > 1$) have dust-to-gas ratios decreasing with R. Evaluating equation (33) explicitly gives

$$\frac{{\rm d}\ln(1+\epsilon)}{{\rm d}\ln R} = \frac{\epsilon}{1-\epsilon}\left[\frac{q}{2} + (\xi-1)p\right]. \tag{34}$$

The special case of constant dust-to-gas ratio requires

$$q = -2(\xi-1)p \quad \text{for constant } \frac{\Sigma_{\rm d}}{\Sigma_{\rm g}}. \tag{35}$$

For nearly isothermal gas and p of order unity, the disc temperature is close to being globally isothermal.

Having specified Σ we can use equation (29) to set the rotation profile

$$\Omega(R) = \Omega_{\rm K}\left[1 - \frac{P}{\Sigma\,(R\Omega_{\rm K})^2}(q + \xi p)\right]^{1/2}, \tag{36}$$

where we have used equation (7).

3.2 Effective disc structure

Using the equilibrium conditions in Section 3.1, we find the radial gradient of the total surface density becomes

$$\widetilde{p} \equiv -\frac{{\rm d}\ln\Sigma}{{\rm d}\ln R} = p - \frac{\epsilon}{1-\epsilon}\left[\frac{q}{2} + (\xi-1)p\right]. \tag{37}$$

Similarly, the radial gradient in the dynamic temperature is

$$\widetilde{q} \equiv -\frac{\partial\ln\widetilde{T}}{\partial\ln R} = q + \frac{\epsilon}{1-\epsilon}\left[\frac{q}{2} + (\xi-1)p\right]. \tag{38}$$

For constant ϵ the term in square brackets is zero, so $(p, q) = (\widetilde{p}, \widetilde{q})$ in this special case.

4 DUSTY DISC–PLANET INTERACTION

We simulate the response of 2D, razor-thin dusty discs described above to an embedded low-mass planet and focus on the associated disc–planet torques. We set $\xi = 1.001$ to model isothermal gas. We adopt $p = q = 0$ as our standard disc profile, which has zero radial pressure gradient and thus no radial drift of particles initially. We fix the dynamic disc temperature such that $\widetilde{h}_0 = 0.05$ for all simulations by letting the gas aspect-ratio vary as $h_{\rm g0} = \sqrt{1+Z}\,\widetilde{h}_0$, where $Z \equiv \Sigma_{\rm d}/\Sigma_{\rm g}$ is the metallicity. This counter-acts the reduction in the effective scale height $\widetilde{H}$ due to dust-loading.

We consider a planet mass of $M_{\rm p} = 6\times10^{-6}\,{\rm M}_*$, which corresponds to a 2 $\rm M_\oplus$ planet orbiting a solar mass star. The planet is held on a fixed Keplerian circular orbit at R_0. The planet potential is switched on smoothly over one orbit. We adopt a fiducial softening length of $r_s = 0.6\widetilde{H}_0 \simeq 2.38r_h$, where $r_h = (M_{\rm p}/3{\rm M}_*)^{1/3}R_0$ is the planet's Hill radius.

Our simulations summarized in Table 1. We primarily vary the Stokes number $T_{\rm stop} \equiv t_{\rm s0}\Omega_{\rm K0}$ and metallicity Z to explore the effect of imperfect dust–gas coupling and dust-loading on disc–planet torques, respectively. We also vary the power-law indices p, q to examine the effect of the background PV and dust-to-gas ratio profiles, and consider the effect numerical resolution.

4.1 Numerical setup

The disc domain is $R \in [0.6, 1.4]R_0$ and $\varphi \in [0, 2\pi]$. We damp all variables towards their initial values in $R \in [0.6, 0.68]R_0$ and $R \in [1.32, 1.4]R_0$ on a time-scale of the local orbital period. The radial boundary ghost cells are kept at their initial states, while azimuthal boundaries are periodic. This setup is similar to Kley et al. (2012).

We use N_R cells logarithmically spaced in R and N_φ cells uniformly spaced in φ. Our standard numerical resolution is such that $\widetilde{H}$ is resolved by (40,20) cells in the radial and azimuthal directions, respectively. This is similar to the resolution adopted by Paardekooper et al. (2010).

We adopt standard configurations for the code PLUTO with linear reconstruction, the HLLC Riemann solver and second-order Runge–Kutta time integration, and enable the FARGO algorithm (Masset 2000a,b) to accelerate the simulations.

Table 1. Summary of disc parameters used in disc–planet simulations. Comments are made relative to the fiducial run.

Run	Σ_d/Σ_g	T_{stop}	(p, q)	$N_R \times N_\varphi$	Comment
Fiducial	0.5	0	(0,0)	720 × 2672	Reference simulation with perfectly coupled particles. Fig. 1.
Decouple	0.5	10^{-3}	(0,0)	720 × 2672	Partially coupled particles. Fig. 2.
LowDust	0.01	10^{-3}	(0,0)	720 × 2672	Reduced dust-loading. Fig. 8.
HighDust	1.0	10^{-3}	(0,0)	720 × 2672	Increased dust-loading. Fig. 8.
FlatPV	0.5	10^{-3}	(1.5,0)	720 × 2672	Zero vortensity gradient (uniform dust-to-gas ratio). Fig. 11.
PPD0	0.5	0	(1,0.5)	720 × 2672	Protoplanetary disc with perfectly coupled dust. Fig. 12.
PPD	0.5	10^{-3}	(1,0.5)	720 × 2672	Protoplanetary disc with imperfectly coupled dust. Fig. 12.
LowRes	0.5	10^{-3}	(0,0)	360 × 1336	Lowered numerical resolution. Fig. 14.
HighRes	0.5	10^{-3}	(0,0)	1440 × 5344	Increased numerical resolution. Fig. 14.

4.2 Torque analyses

The disc-on-planet torque per unit area, or torque density, is defined as

$$\Gamma_\Sigma \equiv \Sigma \frac{\partial \Phi_p}{\partial \phi}, \tag{39}$$

so the total torque acting on the planet is

$$\Gamma = \iint \Gamma_\Sigma R \mathrm{d}R\mathrm{d}\phi. \tag{40}$$

This integration includes the entire disc, i.e. no cut-off is applied near the planet. We also define the torque per unit radius as

$$\frac{\partial \Gamma}{\partial R} = R \int \Gamma_\Sigma \mathrm{d}\phi. \tag{41}$$

We find the effect of dust is to introduce unsteadiness in torques originating from the planet's co-orbital region. To focus the torque analysis in this region, we define the time-averaged torque per unit radius

$$\left\langle \frac{\partial \Gamma}{\partial R} \right\rangle = \frac{1}{T_{avg}} \int_{T_{avg}} \frac{\partial \Gamma}{\partial R} \mathrm{d}t. \tag{42}$$

The time interval T_{avg} is the oscillation period for the total torque (see Section 4.3). This time-averaged torque essentially captures the steady Lindblad or wave torques outside the co-orbital region; removing it thus allow us to focus on the co-rotation torques.

We compare the measured torques to a semi-analytic torque formula adapted from that based on pure gas simulations developed by Paardekooper et al. (2010). In the dust-free limit our models correspond to locally isothermal discs, we thus modify relevant torque formula from Paardekooper et al. to

$$\begin{aligned} \frac{\Gamma}{\Gamma_{ref}} &= \hat{\Gamma}_L + \hat{\Gamma}_c + \hat{\Gamma}_{hs} \\ &= -\left(2.5 - 0.5\widetilde{q} - 0.1\widetilde{p}\right)\left(\frac{0.4}{b}\right)^{0.71} \\ &\quad - 1.4\widetilde{q}\left(\frac{0.4}{b}\right)^{1.26} + 1.1\left(\frac{3}{2} - \widetilde{p}\right)\left(\frac{0.4}{b}\right) \end{aligned} \tag{43}$$

where $b \equiv r_s/\widetilde{H}_0$, and the torque normalization is

$$\Gamma_{ref} = \Sigma_0 R_0^4 \Omega_{K0}^2 \left(\frac{M_p}{M_*}\right)^2 \left(\frac{1}{\widetilde{h}_0^2}\right). \tag{44}$$

The expressions above are identical in form to Paardekooper et al.'s equation 49, but accounts for dust-loading in Σ_0, $\widetilde{H}_0$, $\widetilde{h}_0$ (Section 2.4.3), and the dust-modified effective disc structure (Section 3.2); although there is some uncertainty as to whether the true or dynamic temperature profile should be used (Paardekooper, private communication). Equation (43) includes the (normalized) Lindblad or wave torque Γ_L; the linear co-rotation torque Γ_c; and the non-linear horseshoe drag Γ_{hs}. Note that $\Gamma_c = 0$ in our standard disc model with $p = q = 0$ and constant dust-to-gas ratio.

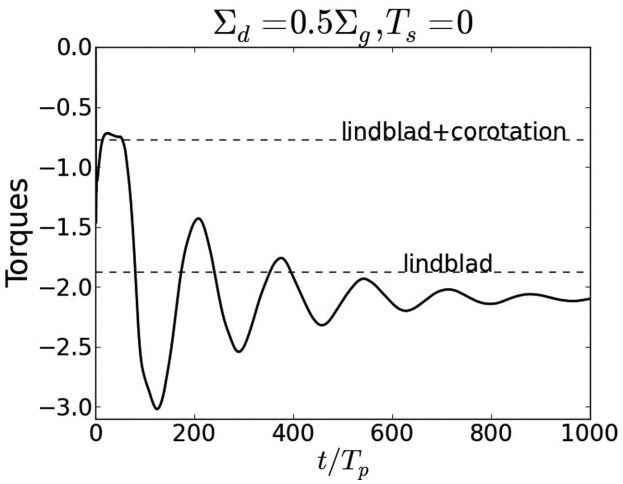

Figure 1. Disc-on-planet torques, normalized by ξ_{ref}, for a 2 $M_\oplus$ planet in the fiducial run with dust-to-gas ratio $Z = 0.5$ and stopping time $T_{stop} = 0$ (solid lines). Horizontal lines are semi-analytic torque values adapted from Paardekooper et al. (2010), where the upper (lower) line corresponds to the total (Lindblad) torques.

4.3 Perfectly coupled dust

We begin with a fiducial run with perfectly coupled dust ($T_{stop} = 0$) but high dust-loading, Z= 0.5. In this case, the system is truly a single fluid and the only effect of dust is to lower the dynamic temperature of the mixture when compared to the pure gas limit.

Fig. 1 shows that resulting total torque agrees well with equation (43) for $\lesssim 50P_0$ when the horseshoe drag remains unsaturated (Paardekooper et al. 2010); and for $t \to \infty$ when the horseshoe drag saturates due to mixing of the co-orbital region, leaving only the Lindblad torques.

This experiment demonstrates that for sufficiently small particles, disc–planet torques are unaffected once dust-loading is accounted for in the torque normalizations, namely in increasing the total surface density and in reducing the disc aspect-ratio.

4.4 Partially coupled dust and torque oscillations

We now allow the dust to be slightly decoupled from the gas by setting $T_{stop} = 10^{-3}$. This decoupled run is compared to the fiducial

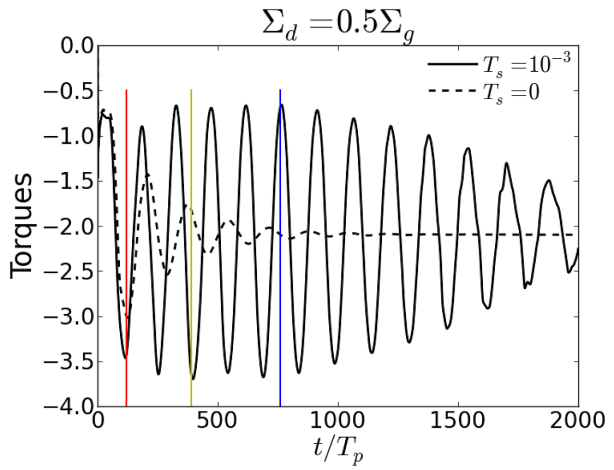

Figure 2. Disc-on-planet torques for a 2 $M_\oplus$ planet in a disc with dust-to-gas ratio $Z = 0.5$ and stopping time $T_{\rm stop} = 0$ (dashed) and $T_{\rm stop} = 10^{-3}$ (solid). The three vertical lines correspond to representative timestamps in Figs 3–6.

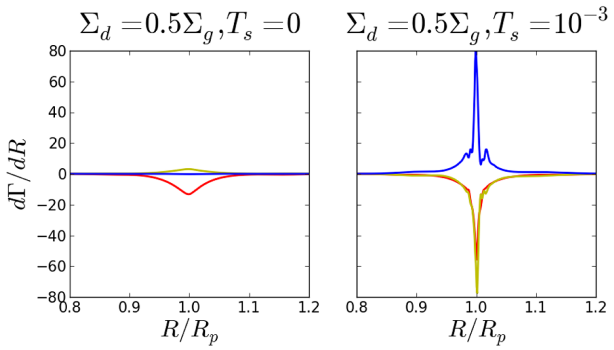

Figure 3. Disc-on-planet torques per unit radius, subtracted by the Lindblad torques, for a 2 $M_\oplus$ planet in a disc with dust-to-gas ratio $Z = 0.5$ and stopping time $T_{\rm stop} = 0$ (left) and $T_{\rm stop} = 10^{-3}$ (right). The three timestamps refer to Fig. 2.

case in Fig. 2. We also extended the simulations to $t = 2000P_0$ to compare their long-term evolution.

In both cases, the average torque is close to the Lindblad-only values. For $T_{\rm stop} = 0$ the torque oscillations immediately damp towards the Lindblad-only values, and reaches a steady state by the end of the simulation. However, in the decoupled run with $T_{\rm stop} = 10^{-3}$, the oscillations are sustained up to ∼1000 orbits before starting to damp. In fact, the oscillation amplitudes reach the unsaturated (full) torque values. The torque remains oscillatory throughout the simulation, but will likely eventually converge to that of the fiducial, perfectly coupled run.

Fig. 3 compares the torque distributions at the representative times shown in Fig. 2. Following the procedure outline in Section 4.2, we subtract the steady Lindblad torques to highlight the difference in the co-rotation region. The figure shows that even a slight dust–gas decoupling can generate and sustain co-rotation torques, leading to oscillatory behaviour.

In Fig. 4, we compare the surface density evolution in the co-orbital region. Although the surface density perturbations are small, as expected for a low-mass planet, they are nevertheless distinct depending on $T_{\rm stop}$. The $T_{\rm stop} = 0$ fiducial run has a relatively smooth surface density distribution. However, in the $T_{\rm stop} = 10^{-3}$ decoupled

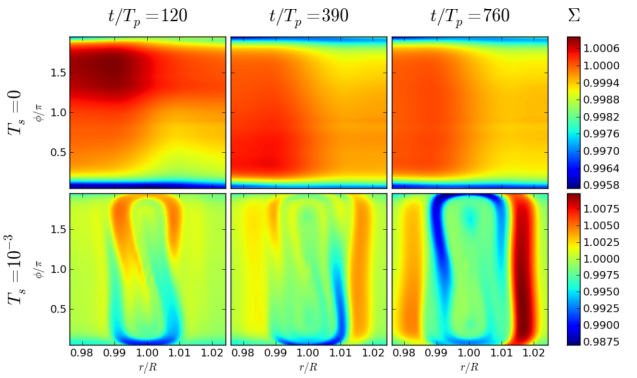

Figure 4. Normalized surface density for a 2 $M_\oplus$ planet in a disc with dust-to-gas ratio $\epsilon_0 = 0.5$ and stopping time $T_{\rm stop} = 0$ (upper) and $T_{\rm stop} = 10^{-3}$ (lower). The three timestamps refer to Fig. 2. The planet is located at the vertical boundaries and the co-orbital flow direction is clockwise. Thus, the flow near the bottom (top) is ahead (behind) the planet.

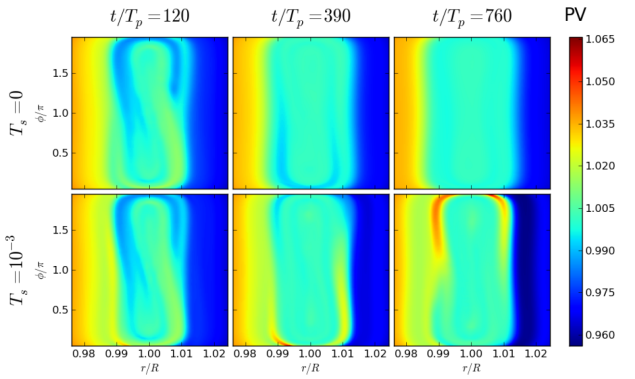

Figure 5. Potential vorticity distribution (PV) for a 2 $M_\oplus$ planet in a disc with dust-to-gas ratio $Z = 0.5$ and stopping time $T_{\rm stop} = 0$ (upper) and $T_{\rm stop} = 10^{-3}$ (lower). The three timestamps refer to Fig. 2.

run, we find a 'bubble' of underdensity (blue in the figure) develops just inside the boundary of the co-orbital region. As it librates, it introduces periodic front-back surface density asymmetries about the planet, and hence sustains a co-rotation torque. Furthermore, we find overdense rings develop outside the co-orbital region, but not in the perfectly coupled case.

4.4.1 Potential vorticity generation from dust–gas misalignment

We note that in pure gas discs the torques originating from the co-orbital region, specifically the horseshoe drag, is known to be related to the PV gradient across the co-rotation region (Paardekooper et al. 2010, see also equation 43). We thus compare the PV distribution between the fiducial and decoupled runs in Fig. 5. Here, the PV is defined as $\zeta = (\hat{z} \cdot \nabla \times \boldsymbol{v} + 2\Omega_{\rm K0})/\Sigma$.

Generally, the PV in the co-orbital region undergoes phase mixing, which leads to the saturation or vanishing of the co-rotational torque (Balmforth & Korycansky 2001). This is the case for $T_{\rm stop} = 0$. However, for $T_{\rm stop} = 10^{-3}$ we find a PV 'blob' develops at the boundary of the co-orbital region, though PV still mixes in the interior. The PV blob corresponds to the surface density bubble identified above.

Interestingly, we find the blob experiences an increase in PV whenever it undergoes horseshoe turns as it encounters the planet. This means that when it completes a libration period, it experiences

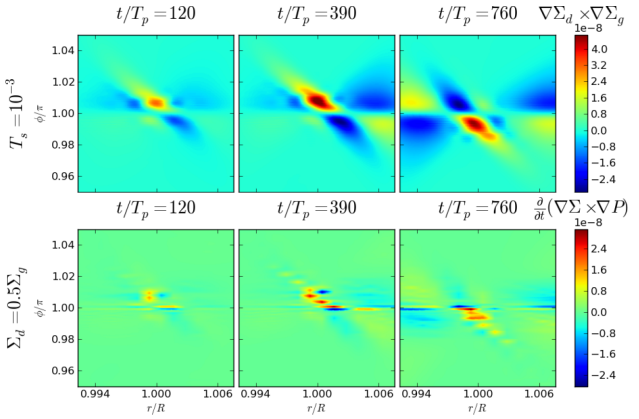

Figure 6. Baroclinic vorticity source $\hat{z} \cdot (\nabla\Sigma_{\rm d} \times \nabla\Sigma_{\rm g})$ and its time derivative in the decoupled run with $Z = 0.5$ and stopping time $T_{\rm stop} = 10^{-3}$. Here, the planet is placed at the centre in each plot. The three timestamps refer to Fig. 2.

two boosts in PV, but it returns to its original orbital radius. We expect no net change in the blob's vorticity, which should be close to the local Keplerian value. Then since $\zeta \propto \Sigma^{-1}$ has increased, its surface density must drop, creating a bubble.

In a 2D disc without shocks, the only source of PV comes from pressure–density misalignment, which is proportional to $\nabla\Sigma_{\rm d} \times \nabla\Sigma_{\rm g}$ (Section 2.5). We plot this PV source in upper panels of Fig. 6 for the decoupled run. By comparing the snapshots with Fig. 5, we see the PV source is positive when the PV blob encounters the planet on a horseshoe turn, so PV is indeed generated through dust–gas misalignment near the planet.

Note that $\nabla\Sigma_{\rm d} \times \nabla\Sigma_{\rm g} = \mathbf{0}$ in the initial disc. However, once the system evolves, this PV source may become non-zero as dust and gas drift relative to each other. We expect this effect to be significant near the planet as a pressure bump can be created by the planet's potential well. Using the 2D versions of equations (9) and (16), with $\xi = 1$ and constant c_s we find

$$\begin{aligned}\frac{\partial}{\partial t}(\nabla\Sigma \times \nabla P) &= \left(\frac{\partial}{\partial t}\nabla\Sigma\right) \times \nabla P + \nabla\Sigma \times \frac{\partial}{\partial t}\nabla P \\ &= \nabla P \times \nabla\left[\nabla \cdot (\Sigma \boldsymbol{v})\right] + \nabla\left[\nabla \cdot (P\boldsymbol{v})\right] \times \nabla\Sigma \\ &\quad + c_s^2 \nabla\Sigma \times \nabla\left[\nabla \cdot (f_{\rm d} t_{\rm s} \nabla P)\right]. \end{aligned} \tag{45}$$

We plot the right-hand side of equation (45) in the lower panels of Fig. 6. (Interestingly, we find the last term is sub-dominant.) It is indeed positive (negative) when the baroclinic source is positive (negative), for a PV surplus (deficit). This suggests a positive feedback loop in generating the PV blob. The blob does not grow indefinitely, however, probably because of numerical diffusion (see Section 4.8).

4.4.2 *Final disc structure*

In Fig. 7, we compare the gas and dust surface density distributions at $t = 2000P_0$. For $T_{\rm stop} = 0$ the dust-to-gas ratio is constant ($Z = 0.5$) so the dust distribution is simply a rescaling of the gas profile. For $T_{\rm stop} = 10^{-3}$, however, a double gap develops in the dust. Although the dust gap is shallow, it is still significant compared to the gas, which only show small fluctuations. This result is consistent with recent studies show that low-mass planets can open dust gaps while leaving the gas relatively unperturbed (Dipierro et al. 2016; Dipierro & Laibe 2017).

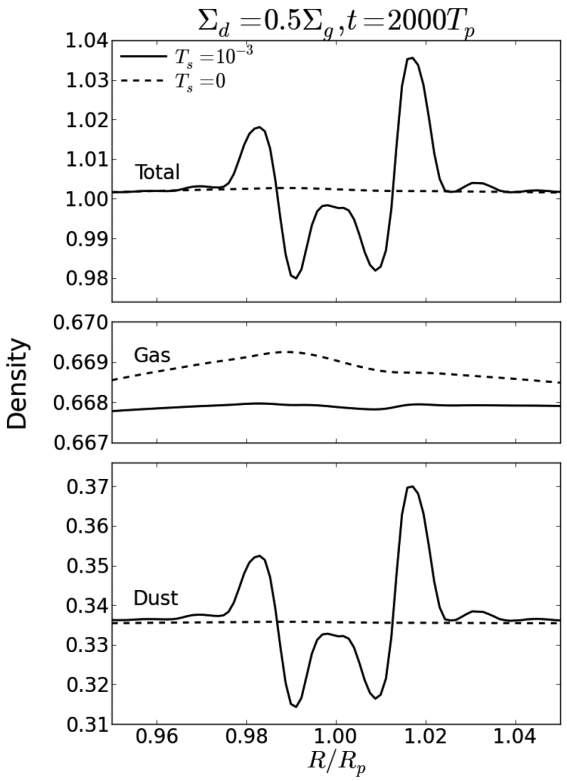

Figure 7. Normalized total (top), gas (middle), and dust (bottom) surface density distributions for a 2 $M_\oplus$ planet in a disc with initial dust-to-gas ratio $Z = 0.5$ and stopping time $T_{\rm stop} = 10^{-3}$ (solid) and $T_{\rm stop} = 0$ (dashed).

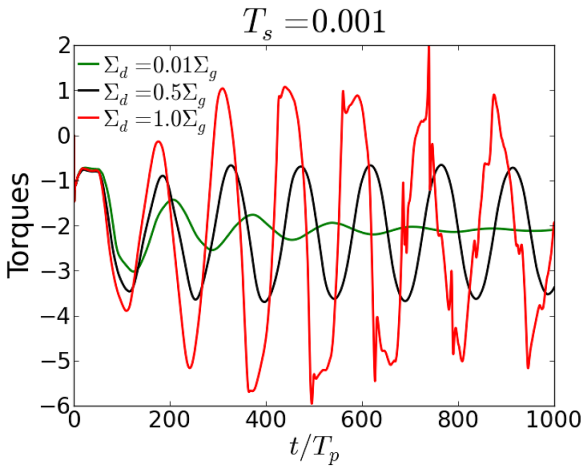

Figure 8. Disc-on-planet torques for a 2 $M_\oplus$ planet in a disc with stopping time $T_{\rm stop} = 10^{-3}$ and different initial dust-to-gas ratios.

4.5 Dust-loading and vortex instability

We now examine the effect of dust-loading by varying the metallicity Z at fixed $T_{\rm stop} = 10^{-3}$. In Fig. 8, we compare the decoupled simulation with $Z = 0.5$ to cases with $Z = 0.01$ and $Z = 1$. The torque evolution for $Z = 0.01$, $T_{\rm stop} = 10^{-3}$ is similar to the fiducial run with $Z = 0.5$, $T_{\rm stop} = 0$. This is expected since the baroclinic term, $|\nabla\Sigma_{\rm d} \times \nabla\Sigma_{\rm g}|$, vanishes as $Z \to 0$. From equation (11), we also expect the magnitude of baroclinity to be proportional to $ZT_{\rm stop}$. Indeed, an additional run with $Z = 5$, $T_{\rm stop} = 10^{-4}$ show similar results to $Z = 0.5$, $T_{\rm stop} = 10^{-3}$.

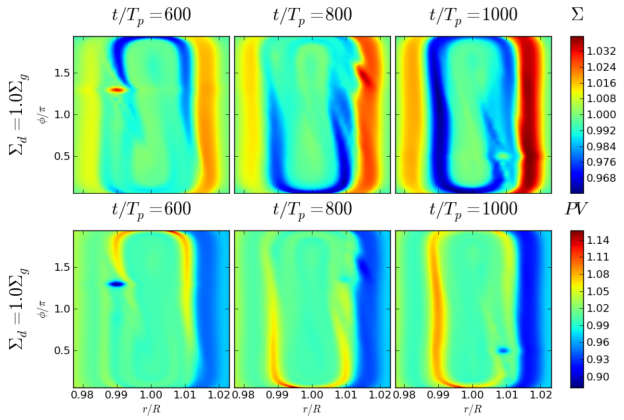

Figure 9. Disc surface density (top) and potential vorticity (bottom) for the high dust-to-gas ratio $Z = 1$ run, showing the development of a co-orbital vortex (red/blue blob in the surface density/PV, respectively).

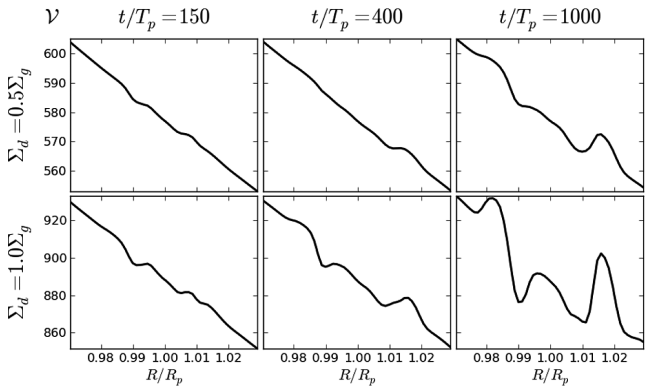

Figure 10. Generalized potential vorticity distribution $\mathcal{V}$ for a 2 $M_\oplus$ planet in a dusty disc with particle stopping time $T_{\rm stop} = 10^{-3}$ and dust-to-gas ratio $Z = 0.5$ (upper) and $Z = 1.0$ (lower).

On the other hand, the torque evolution for the high dust-to-gas ratio disc ($Z = 1$) attains larger oscillation amplitudes than $Z = 0.5$, and eventually develops high-frequency fluctuations on top of the oscillations at $t \gtrsim 500P_0$. We show in Fig. 9 that this is associated with vortex formation at the separatrix of the co-orbital region. A similar phenomenon was observed by Paardekooper et al. (2010) in their pure-gas, adiabatic simulations. They attributed it to the Rossby Wave Instability (RWI; Lovelace et al. 1999; Li et al. 2000) associated with entropy extrema at the separatrix. This can arise from entropy advection when there is a background entropy gradient. In barotropic discs the RWI develops at PV minima (e.g. de Val-Borro et al. 2007, see also Appendix A).

Based on the equivalence between isothermal, dusty gas, and adiabatic pure gas, LY17 argued the relevant quantity for the RWI in isothermal dusty discs is the 'generalized PV'

$$\mathcal{V} \equiv \frac{\kappa^2}{2\Omega\Sigma} \times \left(1 + \frac{\Sigma_{\rm d}}{\Sigma_{\rm g}}\right)^2, \tag{46}$$

where $\kappa^2 = R^{-3}\partial_R\left(R^4\Omega^2\right)$ is the square of the epicyclic frequency. The generalized PV encapsulates both PV (the first factor) and effective entropy (second term). Recall from Section 2.4.2 that the effective entropy of an isothermal, dusty disc is related to the dust-to-gas ratio. Fig. 10 compares the generalized PV profiles for $Z = 0.5$ and $Z = 1$. We indeed find the $Z = 1$ case develops deeper minima in $\mathcal{V}$, which subsequently becomes unstable to vortex formation.

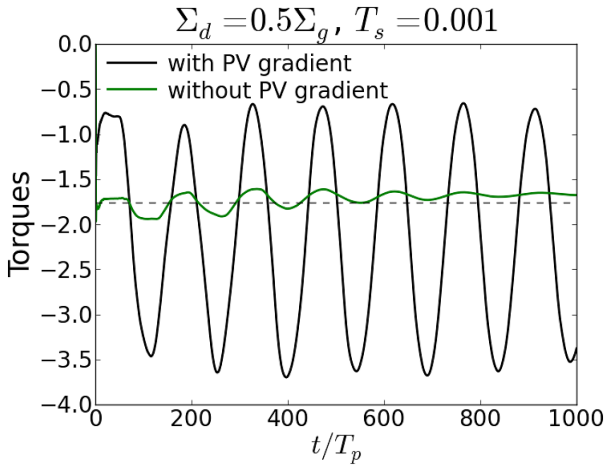

Figure 11. Disc-on-planet torques for a 2 $M_\oplus$ planet in a disc with stopping time $T_{\rm stop} = 10^{-3}$ and different initial PV profile. Horizontal lines correspond to semi-analytic Lindblad torques, $\hat{\Gamma}_{\rm L}$, for locally isothermal discs adapted from Paardekooper et al. (2010).

For our setup the effective entropy is initially uniform because $\Sigma_{\rm d}/\Sigma_{\rm g}$ is constant. Extrema in $\mathcal{V}$ at the separatrices thus arise from (i) advection of the background PV and/or (ii) baroclinic PV and effective entropy generation due to $|\nabla\Sigma_{\rm d} \times \nabla\Sigma_{\rm g}| \neq 0$. To determine which effect is responsible, we ran a case with $Z = 1$, $T_{\rm stop} = 0$, where baroclinity is absent, and found no vortex formation. Thus, in the case with $Z = 1$, $T_{\rm stop} = 10^{-3}$, extrema in $\mathcal{V}$ is associated with the baroclinic source for PV and effective entropy.

4.6 Discs with flat potential vorticity profiles

Here, we consider a disc model with $p = 1.5$ so the initial PV (approximately $\propto R^{3/2-p}$) is nearly uniform. We choose $q = -0.003$ so the true temperature increases slightly outwards to maintain a constant dust-to-gas ratio. These parameters imply vanishing co-rotation torques initially.

In Fig. 11, we plot the torques measured in this flat PV run, in comparison with decoupled run with a PV gradient, and the analytic Lindblad torque value. The oscillation amplitudes are significantly smaller, and the total torque remains close to the Lindblad-only values. This experiment demonstrates that the sustained oscillations requires an initial PV gradient, i.e. a non-vanishing initial co-rotation torque (specifically the horseshoe drag). In that case the initial advection of PV across horseshoe turns, thereby creating a PV surplus, feeds the baroclinic source, which further generates PV.

4.7 Protoplanetary disc models

We now consider a disc model with $p = 1$, $q = 0.5$, which are typical values for protoplanetary discs. In addition to a PV gradient, this model also contains a temperature gradient and an initially non-uniform dust-to-gas ratio. Fig. 12 compares the disc–planet torques in this model for perfectly coupled and partially coupled dust. As before, the $T_{\rm stop} = 10^{-3}$ run sustains larger amplitude torque oscillations than the $T_{\rm stop} = 0$ run; although oscillations in the former case begins to damp after $t \sim 400P_0$, unlike the case with $p = q = 0$ (Fig. 2).

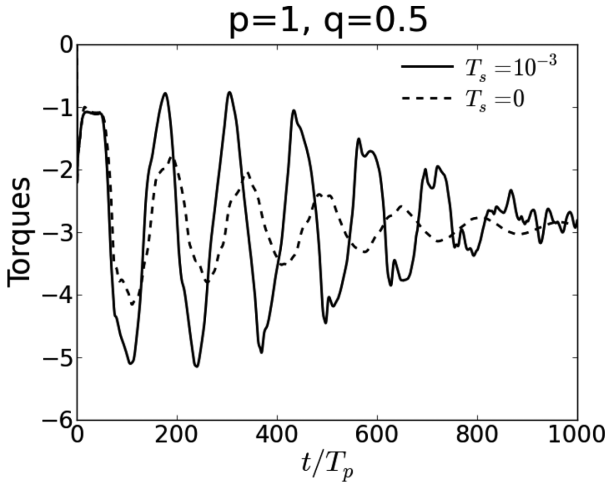

Figure 12. Disc-on-planet torques for a 2 $M_\oplus$ planet in a disc with $p = 1$, $q = 0.5$. The initial dust-to-gas ratio and stopping time at $R = 1$ is $Z = 0.5$ and $T_{\rm stop} = 10^{-3}$ (solid), $T_{\rm stop} = 0$ (dashed).

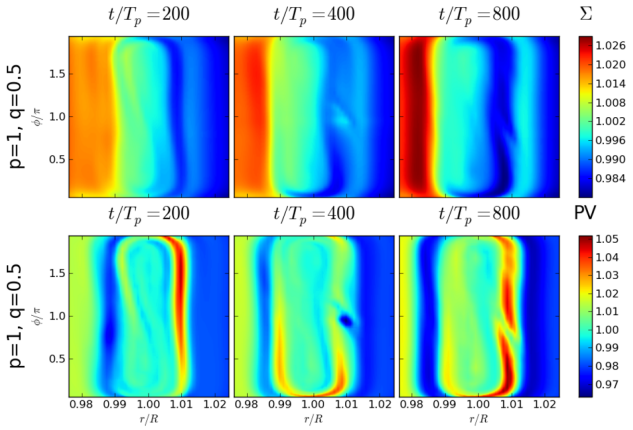

Figure 13. Snapshots of normalized surface density (top) and PV (bottom) for the $p = 1$, $q = 0.5$, $T_{\rm stop} = 10^{-3}$ case shown in Fig. 12.

Interestingly, on longer time-scales, Fig. 13 shows that the PPD model with $T_{\rm stop} = 10^{-3}$ develops a vortex at the boundary of the co-orbital region, though this did not occur in the $p = q = 0$ run. The advection of dust-to-gas ratio through horseshoe turns in the presence of a background gradient in $\Sigma_{\rm d}/\Sigma_{\rm g}$ likely contributes to gradients in the disc's effective entropy at the co-orbital boundary, in addition to entropy generation from baroclinity. This effect would favour the RWI in the case with $p = 1$, $q = 0.5$.

However, unlike the run with high dust-to-gas ratios (Section 4.5), here the vortex is a transient feature; dissipating as the co-orbital region undergoes phase mixing. The total torque then converges to a nearly constant value similar to the $T_{\rm stop} = 0$ case.

4.8 Numerical resolution

Our simulations are carried out in the inviscid limit. Thus, the smallest scale is always the grid scale. Numerical diffusion could be important in co-orbital dynamics, specifically the separatrices, where large gradients can develop.

In Fig. 14, we repeat the decoupled run at half and double the standard resolution (40, 20 cells per $\widetilde{H}$ in r, φ, respectively). For $t \lesssim 100P_0$ the linear torques are well converged. For $t \gtrsim 100P_0$ at

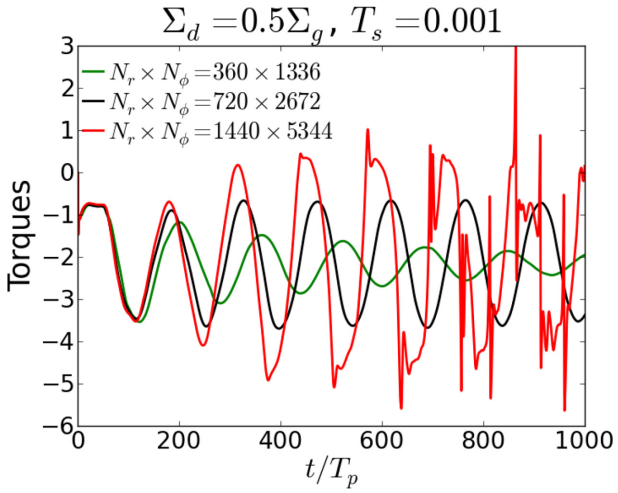

Figure 14. Disc-on-planet torques for a 2 $M_\oplus$ planet in a disc with stopping time $T_{\rm stop} = 10^{-3}$ and different resolutions.

low-resolution numerical diffusion causes efficient PV mixing in the co-orbital region, despite baroclinic source, and the oscillation damps. This effect is mitigated at high resolution, resulting in larger torque amplitudes. The torque magnitudes can exceed the initial values, and even becomes positive at times.

However, we also find vortex formation in the high-resolution case due to the RWI, because the large gradients at the separatrices are better resolved. It is thus unclear if seeking true convergence is meaningful in these inviscid simulations. We emphasize that the dusty baroclinic generation of PV (and sustained co-orbital torques) is a physical effect, but require sufficient resolution to counter PV mixing/ numerical diffusion.

The different resolutions presented here could mimic discs with different levels of a background turbulent viscosity. As such, the dust-induced co-orbital torques and RWI would only occur in laminar 'dead zones' of protoplanetary discs. This is consistent with considering a high-metallicity disc in the first place, since only a low level of turbulence would allow dust-settling (Takeuchi & Lin 2002).

5 SUMMARY AND DISCUSSION

In this paper, we implement a new, dust-free model of dusty gas developed by Lin & Youdin (2017) into the PLUTO hydrodynamics code. It assumes the dust particles are small enough so that their stopping time is sufficiently short to treat the dusty gas as a single-phase fluid. The model allows for a slight decoupling between gas and dust by accounting for dust–gas relative drift via a source term in an effective energy equation. In this first numerical application of the Lin & Youdin's dust-free framework, we utilize the code to revisit disc–planet interaction in the limit of high dust-to-gas ratios and focus on disc–planet torques. We mainly consider the effect of stopping times $T_{\rm stop}$ (or particle size) and dust-loading Z (or metallicity).

For perfectly coupled dust ($T_{\rm stop}= 0$), the disc–planet torques match to the torque formula adapted from Paardekooper et al. (2010), which are based on pure gas simulations. We find a good match when the horseshoe drag is still unsaturated, as well when the total torque converges to the Lindblad-only values ($t \gtrsim 1000$ orbits). The effect of dust-loading can be absorbed into the torque normalization, namely a reduction in the effective disc scale height

and in contributing to the total disc mass. Runs with finite stopping time but low metallicity (e.g. $T_{\rm stop} = 10^{-3}$, $Z = 0.01$) behave similarly to perfectly coupled dust at higher metallicity, in that torques immediately damp towards the Lindblad-only values.

However, for finite stopping time *and* high metallicity, e.g. $T_{\rm stop} = 10^{-3}$, $Z = 0.5$, the torque oscillation amplitudes do not damp until after ∼1000 orbits (cf. the run with perfectly coupled dust). The torques remain oscillatory until at least ∼2000 orbits, although it appears to be converging towards the Lindblad values. We traced this phenomenon to PV generation from the misalignment between dust and gas surface densities in the planet's co-orbital region. A PV blob, corresponding to a surface density 'bubble', is created by the initial condition near the separatrices of the co-orbital region, and experiences a baroclinic PV boost whenever it passes by the planet via horseshoe turns. As the PV blob librates at the co-orbital boundary, it introduces periodic surface density asymmetries in front of and behind the planet, which translates to sustained oscillatory co-orbital torques. The PV blob eventually dissipates, possibly due to numerical diffusion and/or PV mixing in the co-orbital region.

Increasing the disc metallicity at fixed stopping time, e.g. $T_{\rm stop} = 10^{-3}$, $Z = 1$, leads to vortex formation in the co-orbital region. This introduces high-frequency variability in the disc torques. In previous, pure gas, adiabatic simulations, co-orbital vortex formation was attributed to the RWI associated with strong entropy gradients at the separatrices (Paardekooper et al. 2010). In general the RWI is related to extrema in PV and/or entropy profiles. In isothermal, dusty discs the relevant quantity is the generalized PV, $\mathcal{V} = (\kappa^2/2\Omega\Sigma)(1 + \Sigma_{\rm d}/\Sigma_{\rm g})^2$, which captures both the PV and effective entropy of isothermal dusty gas. Analysis of the $\mathcal{V}$ profiles in the unstable cases show that prior to vortex formation, extrema in $\mathcal{V}$ indeed develops in the co-orbital region.

We also consider two additional disc models: one with zero PV gradient initially and a protoplanetary disc model with non-zero gradients in PV, temperature, and initial dust-to-gas ratio. In the flat PV disc, the torques immediately jump to the Lindblad torque and does not change much after. This is consistent with the previous simulations, which show a PV boost occurs if there is an Eulerian PV perturbation when a fluid parcel undergoes horseshoe turns. An initial PV surplus cannot develop if PV is globally flat. This simulation shows that sustained oscillatory torques require a background PV gradient. In the protoplanetary disc model, we again find sustained torque oscillations, but at late times a high-frequency torque component develops due to vortex formation in the co-orbital region. However, this vortex appears to be transient, dissipating within the simulation time-scale, leaving only the Lindblad torques to remain.

5.1 Implications of dusty disc–planet interaction

Our main result is that low-mass planets in dusty discs may experience extended periods of oscillatory torques acting on them. This could lead to growth in the planet's eccentricity. This effect requires sufficiently high dust-loading and/or large particles. If a planet migrates into the inner disc with high dust-to-gas ratio and large particles – a typical outcome of particle drift (e.g. Kanagawa et al. 2017) – then oscillatory torques may develop and introduce planet eccentricity. Alternatively, once particles in the disc surrounding the planet grows beyond some size, finite dust–gas coupling may again introduce oscillatory torques.

We also find vortex formation in the co-orbital region in some cases. The effect of co-orbital vortices on vortex formation is less clear, and is best address through direct numerical simulations. However, these vortices are expected to act as dust traps (Lyra & Lin 2013), and may lead to additional planetesimal and hence planet formation, which would further complicate the orbital migration of the original planet.

5.2 Caveats and outlooks

Our simulations motivate the study of dust-rich disc–planet interaction in detail. In order to follow up the possible implications discussed above, several improvements needs to be made in future work.

We constructed special disc profiles in order to initialize our simulations in exact equilibrium. In fact, we mostly considered discs without an initial pressure gradient, i.e. no particle drift. In general, however, the disc may be evolving due to dust–gas interaction (Kanagawa et al. 2017). Future studies should consider more general, possibly non-equilibrium initial conditions. In particular, a global particle and/or gas mass flux across the planet's co-orbital region will likely contribute to the desaturation of co-orbital torques (McNally et al. 2017).

In this first study, we fixed the planet's orbit and simply measured the disc–planet torques. To see how a planet actually migrates in response to these torques, specifically whether or not it can experience eccentricity growth, we require a live planet, i.e. an orbit integrator. This problem, however, will likely require high numerical resolutions.

Future studies should also consider fully 3D, stratified disc models. This is because dust–gas drag – a key factor in the torque evolution – depends on the local density (equation 3). In a 3D disc the stopping time increases away from the mid-plane; while the dust-to-gas ratio or local metallicity drops with height. This height dependence may not be properly captured in our 2D disc models, in which we simply replace the densities by surface densities. Three-dimensional disc models also allow for explicit modelling of hydrodynamic turbulence such as that due to the Vertical Shear Instability (Nelson, Gressel & Umurhan 2013). This is expected to be important for the co-orbital dynamics considered here as it provides an effective viscosity. However, such 3D numerical simulations are prohibitively expensive at the present time.

ACKNOWLEDGEMENTS

This work is supported by the Theoretical Institute for Advanced Research in Astrophysics (TIARA) based in the Academia Sinica Institute for Astronomy and Astrophysics (ASIAA). JWC is supported by the 2017 ASIAA Summer Student Programm, where this project began. All simulations were carried out on the TIARA High Performance Computing cluster.

REFERENCES

Alexander R., Pascucci I., Andrews S., Armitage P., Cieza L., 2014, Protostars and Planets VI. Univ. Arizona Press, Tucson, AZ, p. 4756
ALMA Partnership, 2015, ApJ, 808, L3
Andrews S. M. et al., 2016, ApJ, 820, L40
Ayliffe B. A., Laibe G., Price D. J., Bate M. R., 2012, MNRAS, 423, 1450
Bae J., Zhu Z., Hartmann L., 2016, ApJ, 819, 134
Bae J., Zhu Z., Hartmann L., 2017, ApJ, 850, 201
Bai X.-N., 2016, ApJ, 821, 80
Bai X.-N., Stone J. M., 2010, ApJS, 190, 297
Balmforth N. J., Korycansky D. G., 2001, MNRAS, 326, 833
Balsara D. S., Tilley D. A., Rettig T., Brittain S. D., 2009, MNRAS, 397, 24
Barker A. J., Latter H. N., 2015, MNRAS, 450, 21

Baruteau C., Masset F., 2008a, ApJ, 672, 1054
Baruteau C., Masset F., 2008b, ApJ, 678, 483
Baruteau C., Meru F., Paardekooper S.-J., 2011a, MNRAS, 416, 1971
Baruteau C., Fromang S., Nelson R. P., Masset F., 2011b, A&A, 533, A84
Baruteau C. et al., 2014, Protostars and Planets VI. Univ. Arizona Press, Tucson, AZ , p. 667.
Baruteau C., Bai X., Mordasini C., Mollière P., 2016, Space Sci. Rev., 205, 77
Benítez-Llambay P., Pessah M. E., 2018, ApJ, 855, L28
Benítez-Llambay P., Masset F., Koenigsberger G., Szulágyi J., 2015, Nature, 520, 63
Carrera D., Johansen A., Davies M. B., 2015, A&A, 579, A43
Cieza L. A. et al., 2017, ApJ, 851, L23
de Val-Borro M., Artymowicz P., D'Angelo G., Peplinski A., 2007, A&A, 471, 1043
Dipierro G., Laibe G., 2017, MNRAS, 469, 1932
Dipierro G., Price D., Laibe G., Hirsh K., Cerioli A., Lodato G., 2015, MNRAS, 453, L73
Dipierro G., Laibe G., Price D. J., Lodato G., 2016, MNRAS, 459, L1
Dong R., Li S., Chiang E., Li H., 2017, ApJ, 843, 127
Flock M., Nelson R. P., Turner N. J., Bertrang G. H.-M., Carrasco-González C., Henning T., Lyra W., Teague R., 2017, ApJ, 850, 131
Fouchet L., Maddison S. T., Gonzalez J.-F., Murray J. R., 2007, A&A, 474, 1037
Fu W., Li H., Lubow S., Li S., 2014a, ApJ, 788, L41
Fu W., Li H., Lubow S., Li S., Liang E., 2014b, ApJ, 795, L39
Fung J., Chiang E., 2017, ApJ, 839, 100
Goldreich P., Tremaine S., 1980, ApJ, 241, 425
Goldreich P., Ward W. R., 1973, ApJ, 183, 1051
Gonzalez J.-F., Laibe G., Maddison S. T., 2017, MNRAS, 467, 1984
Guilet J., Baruteau C., Papaloizou J. C. B., 2013, MNRAS, 430, 1764
Jacquet E., Balbus S., Latter H., 2011, MNRAS, 415, 3591
Jin S., Li S., Isella A., Li H., Ji J., 2016, ApJ, 818, 76
Johansen A., Youdin A., 2007, ApJ, 662, 627
Johansen A., Blum J., Tanaka H., Ormel C., Bizzarro M., Rickman H., 2014, Protostars and Planets VI. Univ. Arizona Press, Tucson, AZ, p. 547
Kanagawa K. D., Ueda T., Muto T., Okuzumi S., 2017, ApJ, 844, 142
Kley W., Müller T. W. A., Kolb S. M., Benítez-Llambay P., Masset F., 2012, A&A, 546, A99
Koller J., Li H., Lin D. N. C., 2003, ApJ, 596, L91
Laibe G., Price D. J., 2014, MNRAS, 440, 2136
Li H., Finn J. M., Lovelace R. V. E., Colgate S. A., 2000, ApJ, 533, 1023
Li H., Li S., Koller J., Wendroff B. B., Liska R., Orban C. M., Liang E. P. T., Lin D. N. C., 2005, ApJ, 624, 1003
Li H., Lubow S. H., Li S., Lin D. N. C., 2009, ApJ, 690, L52
Lin M.-K., Papaloizou J. C. B., 2010, MNRAS, 405, 1473
Lin M.-K., Papaloizou J. C. B., 2011, MNRAS, 415, 1426
Lin M.-K., Youdin A. N., 2015, ApJ, 811, 17
Lin M.-K., Youdin A. N., 2017, ApJ, 849, 129
Lovelace R. V. E., Li H., Colgate S. A., Nelson A. F., 1999, ApJ, 513, 805
Lyra W., Lin M.-K., 2013, ApJ, 775, 17
Lyra W., Johansen A., Klahr H., Piskunov N., 2009, A&A, 493, 1125
Masset F., 2000a, A&AS, 141, 165
Masset F. S., 2000b, in Garzón G., Eiroa C., de Winter D., Mahoney T. J., eds, ASP Conf. Ser. Vol. 219, Disks, Planetesimals, and Planets. Astron. Soc. Pac., San Francisco, p. 75
Masset F. S., Casoli J., 2010, ApJ, 723, 1393
Masset F. S., Papaloizou J. C. B., 2003, ApJ, 588, 494
McNally C. P., Nelson R. P., Paardekooper S.-J., Gressel O., Lyra W., 2017, MNRAS, 472, 1565
Mignone A., Bodo G., Massaglia S., Matsakos T., Tesileanu O., Zanni C., Ferrari A., 2007, ApJS, 170, 228
Mignone A., Flock M., Stute M., Kolb S. M., Muscianisi G., 2012, A&A, 545, A152
Miniati F., 2010, J. Comput. Phys., 229, 3916
Nelson R. P., Papaloizou J. C. B., 2003, MNRAS, 339, 993
Nelson R. P., Gressel O., Umurhan O. M., 2013, MNRAS, 435, 2610
Paardekooper S.-J., 2014, MNRAS, 444, 2031
Paardekooper S.-J., Mellema G., 2004, A&A, 425, L9
Paardekooper S.-J., Mellema G., 2006, A&A, 459, L17
Paardekooper S.-J., Mellema G., 2008, A&A, 478, 245
Paardekooper S.-J., Baruteau C., Crida A., Kley W., 2010, MNRAS, 401, 1950
Pepliński A., Artymowicz P., Mellema G., 2008, MNRAS, 386, 179
Picogna G., Kley W., 2015, A&A, 584, A110
Price D. J., Laibe G., 2015, MNRAS, 451, 813
Rafikov R. R., 2002, ApJ, 572, 566
Ragusa E., Dipierro G., Lodato G., Laibe G., Price D. J., 2017, MNRAS, 464, 1449
Rosotti G. P., Juhasz A., Booth R. A., Clarke C. J., 2016, MNRAS, 459, 2790
Stoll M. H. R., Picogna G., Kley W., 2017, A&A, 604, A28
Takeuchi T., Lin D. N. C., 2002, ApJ, 581, 1344
Terquem C. E. J. M. L. J., 2003, MNRAS, 341, 1157
Testi L. et al., 2014, Protostars and Planets VI. Univ. Arizona Press, Tucson, AZ, p. 339.
Tricco T. S., Price D. J., Laibe G., 2017, MNRAS, 471, L52
Uribe A. L., Klahr H., Flock M., Henning T., 2011, ApJ, 736, 85
van Boekel R. et al., 2017, ApJ, 837, 132
van der Marel N. et al., 2013, Science, 340, 1199
van der Plas G., Ménard F., Canovas H., Avenhaus H., Casassus S., Pinte C., Caceres C., Cieza L., 2017, A&A, 607, A55
Weidenschilling S. J., 1977, MNRAS, 180, 57
Whipple F. L., 1972, in Elvius A., ed., From Plasma to Planet. Wiley Interscience Division, New York, p. 211
Yang C.-C., Johansen A., 2016, ApJS, 224, 39
Yang C.-C., Johansen A., Carrera D., 2017, A&A, 606, A80
Youdin A. N., Goodman J., 2005, ApJ, 620, 459
Youdin A., Johansen A., 2007, ApJ, 662, 613
Zhang H., Yuan C., Lin D. N. C., Yen D. C. C., 2008, ApJ, 676, 639
Zhu Z., Nelson R. P., Dong R., Espaillat C., Hartmann L., 2012, ApJ, 755, 6
Zhu Z., Stone J. M., Rafikov R. R., Bai X.-n., 2014, ApJ, 785, 122

APPENDIX A: DUST-TRAPPING AT PLANETARY GAP EDGES

We simulate the response of a 2D, razor-thin dusty disc to massive planets such that the disc structure in dust is significantly perturbed. Here, for the disc parameters we use $p = 1$, $q = -0.002$ to obtain a uniform dust-to-gas ratio of $\Sigma_d/\Sigma_g = 0.01$. As before we use $\xi = 1.001$, so gas disc is effectively isothermal in both structure and thermal response. The reference gas temperature is such that $h_{g0} = 0.05$. Since $\Sigma_d \ll \Sigma_g$, there is no difference between the true and dynamic (dust-modified) temperature. We set the reference stopping time to $T_{stop} = 0.007$. This setup is similar to recent explicit dust-plus-gas simulations performed by Dong et al. (2017). However, unlike Dong et al., we neglect gas viscosity and turbulent dust diffusion.

The disc domain is $R \in [0.4, 2.5]R_0$ and $\varphi \in [0, 2\pi]$ with resolution of $N_R \times N_\varphi = 384 \times 768$. As in Section 4, we use unperturbed boundaries with radial buffer zones in $R \in [0.4, 0.52]R_0$ and $R \in [2.2, 2.5]R_0$.

A1 Dust rings

Fig. A1 shows the normalized gas and dust surface densities at $t = 700P_0$ for a planet of mass $M_p = 3 \times 10^{-5}$ M_*, or $M_p = 10$ $M_\oplus$ if $M_* = M_\odot$. While a single, shallow gas gap is carved with only ~20 per cent depletion in gas; a double, deep dust gap is formed with almost complete depletion. The dust displays a multiringed structure associated with the gas gap edges and the co-orbital (horseshoe) region of the planet. In particular, the co-orbital material itself shows a double-ringed structure. These features are very similar to that

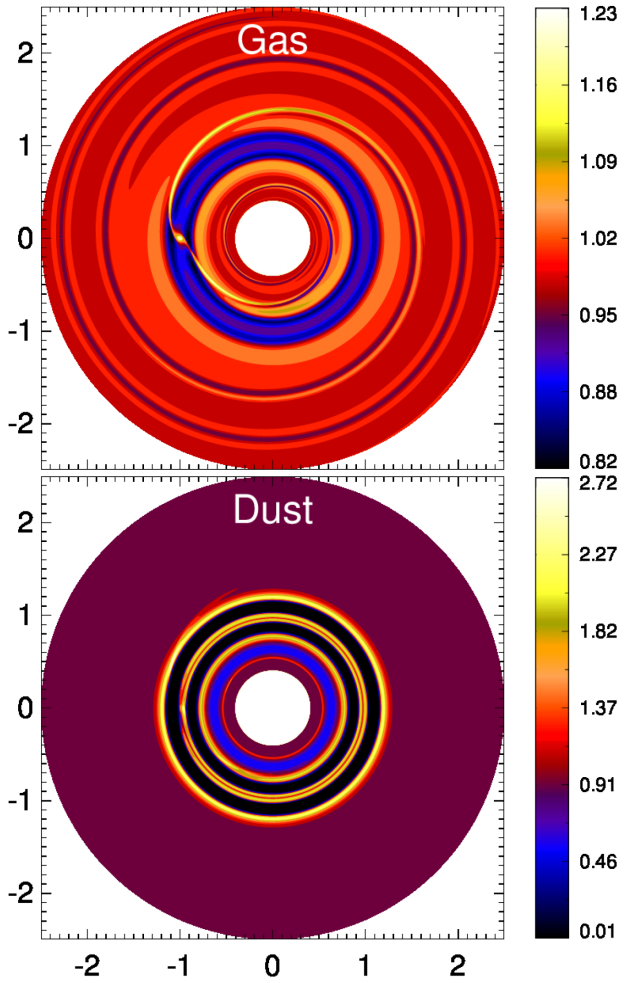

Figure A1. Gas (top) and dust (bottom) response to an embedded planet with mass of 10 $M_\oplus$ around a star of mass $M_\odot$. The gas and dust surface densities $\Sigma_{d,\,g}$ are normalized by their initial values.

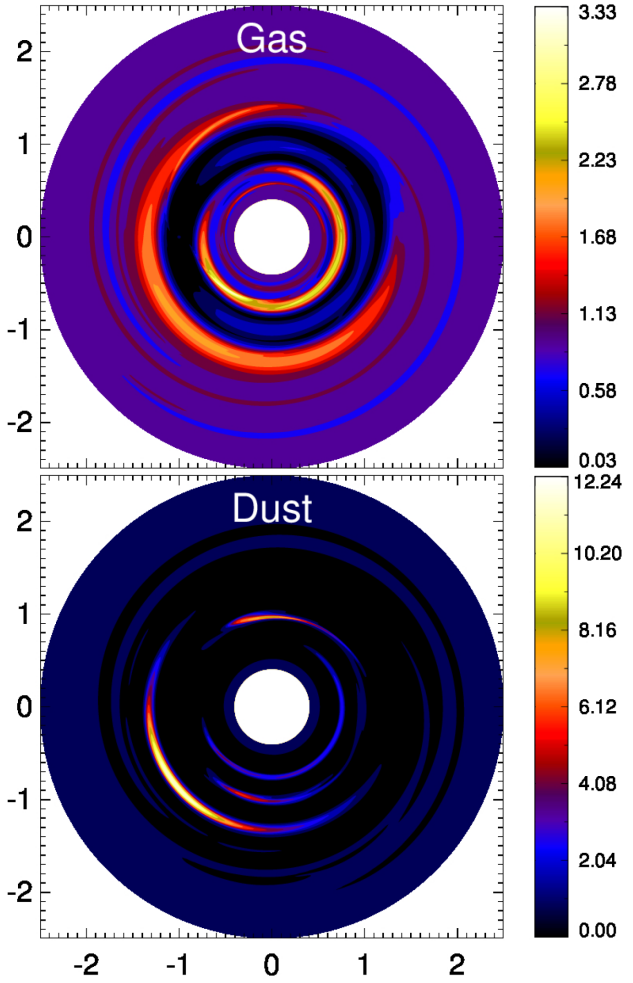

Figure A2. Same as Fig. A1 but with a planet mass $M_p = 100\ M_\oplus$.

obtained by Dong et al. (2017, see their fig. 1) in their two-phase simulations.

A2 Dusty vortex

We repeat the above simulation with $M_p = 3 \times 10^{-4}\ M_*$; equivalent to 100 $M_\oplus$ or a Saturn-mass planet around a Solar mass star. Fig. A2 shows the gas and dust distribution at $t = 500P_0$. For this planet mass a partial gas gap forms, which subsequently becomes unstable to the RWI (Lin & Papaloizou 2010), which leads to large-scale vortex formation at the gap edges. The dust is efficiently trapped by the vortices in both radius and azimuth (Lyra & Lin 2013), resulting in a much higher concentration than the gas overdensity. The dust gap is also wider than the gas gap, probably due to dust-collection into the outer vortex.

APPENDIX B: STREAMING INSTABILITY WITH ONE FLUID

The streaming instability (SI) is an axisymmetric, linear dust-drag instability (Youdin & Goodman 2005; Jacquet et al. 2011). SI relies on the back-reaction of dust-drag on gas, and thus is most efficient in dust-rich discs ($\rho_d \gtrsim \rho_g$). This is especially true for tightly coupled, small particles with $T_{stop} \ll 1$ (Carrera, Johansen & Davies 2015; Yang, Johansen & Carrera 2017).

Linear SI growth rates may be calculated analytically from a full two-fluid treatment of dusty gas (Youdin & Goodman 2005). In the strong-drag limit, SI growth rates may also be obtained from the one fluid, approximate framework considered here (LY17). This provides a means to test the implementation of the diffusion-like term to model dust–gas drag.

B1 Unstratified global equilibria

In order to compare with the analytical calculations of SI, we consider axisymmetric, 3D discs but neglect vertical stratification in the initial equilibrium. This is done by ignoring the z-dependence of the gravitational potential.

The equilibrium density and velocity profiles physically represent conditions near the disc mid-plane. We thus set

$$\rho_g = \frac{\Sigma_g(R)}{\sqrt{2\pi}\,H_g(R)} \propto R^{-p+q/2-3/2}, \tag{B1}$$

for consistency with stratified discs considered in Appendix Section C, and recall Σ_g is given by equation (31).

The total density is $\rho = \rho_g(1+\epsilon)$, and the initial dust-to-gas ratio $\epsilon(R)$ is chosen to satisfy thermal equilibrium, $\partial_R\,(R f_d t_s \partial_R P) = 0$, similarly to the razor-thin disc in Section 3.1. This results in the

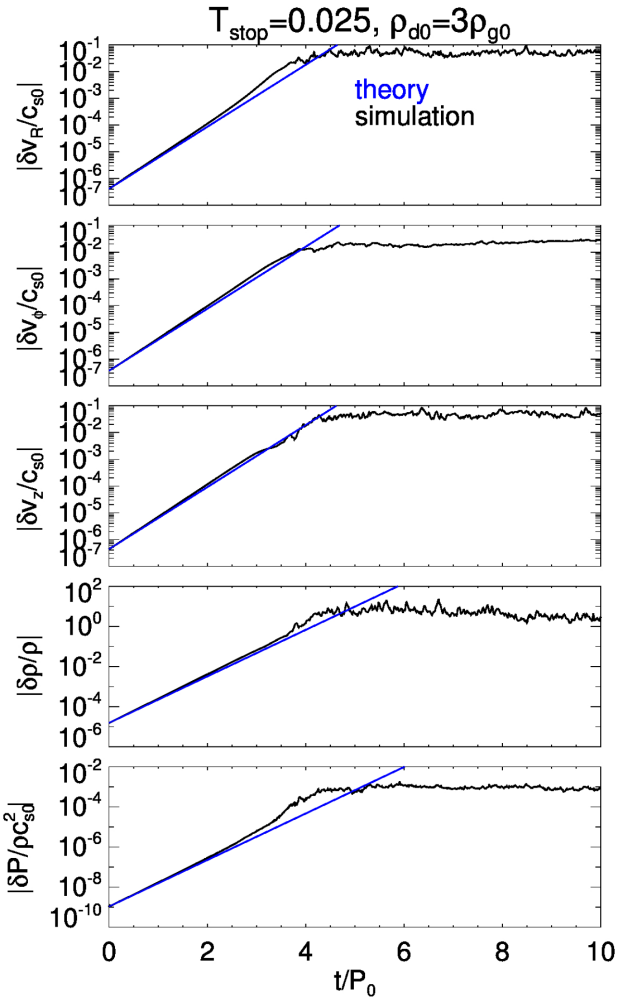

Figure B1. Growth of the streaming instability in run A (see Table B1). The evolution in the maximum deviation from initial conditions are plotted (black) and compared to the expected linear growth of SI (blue).

constraint

$$\frac{\epsilon}{(1+\epsilon)^2} c_s(R)\rho_g^{\xi-1}(R) = \text{constant} \tag{B2}$$

for power-law discs; assuming $\partial_R P \neq 0$, as required for SI (see below). We thus set the dust-to-gas ratio via

$$\frac{\epsilon(R)}{[1+\epsilon(R)]^2} = \frac{\epsilon_0}{(1+\epsilon_0)^2}\left[\frac{c_{s0}}{c_s(R)}\right]\left[\frac{\rho_{g0}}{\rho_g(R)}\right]^{\xi-1}.$$

Then

$$\frac{\mathrm{d}\ln(1+\epsilon)}{\mathrm{d}\ln R} = \frac{\epsilon}{1-\epsilon}\left\{\frac{q}{2} + (\xi-1)\left[p + \left(\frac{3}{2} - \frac{q}{2}\right)\right]\right\}, \tag{B3}$$

The special case of a uniform dust-to-gas ratio is only possible if

$$q = \frac{2(\xi-1)}{\xi-2}\left(p+\frac{3}{2}\right) \quad \text{for constant } \frac{\rho_\mathrm{d}}{\rho_\mathrm{g}}. \tag{B4}$$

We choose $\xi = 1.001$ and $p = 1$, and set $q \simeq -0.005$ in accordance with equation (B4) to obtain a constant ϵ.

The disc rotation profile is given via

$$R\Omega^2 = R\Omega_\mathrm{K}^2 + \frac{1}{\rho}\frac{\mathrm{d}P}{\mathrm{d}R}. \tag{B5}$$

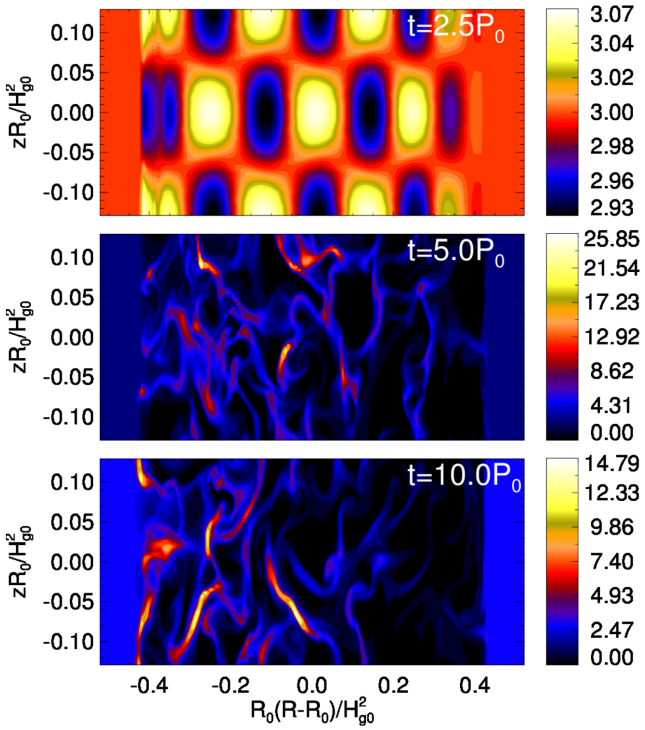

Figure B2. Evolution of dust-to-gas ratio for run A with $T_\mathrm{stop} = 0.025$ ($\tau_\mathrm{s} = 0.1$) at 2.5 orbits (top, end of linear phase), 5 orbits (middle, saturated state), and 10 orbits (bottom, end of simulation). Notice the inwards migration of dust clumps due to the global radial pressure gradient.

SI requires particle drift in the initial equilibrium, which translates to a non-zero radial pressure gradient. In the literature it is common use the parametrization

$$\eta \equiv -\frac{1}{2\rho_\mathrm{g} R\Omega_\mathrm{K}^2}\frac{\partial P}{\partial R}. \tag{B6}$$

The reference temperature is chosen such that $h_{g0} = 0.1$, giving a dimensionless pressure gradient $\eta_0 \simeq 0.0125$ for the fiducial disc model.

B2 Simulation setup

We initialize the simulation with axisymmetric Eulerian perturbations in $\boldsymbol{Q} = (\rho, \boldsymbol{v}, P)$ in the form

$$\delta\boldsymbol{Q} = \mathrm{Re}\left[\widetilde{\boldsymbol{Q}}\exp\mathrm{i}\,(k_x R + k_z z - \sigma t)\right]. \tag{B7}$$

Here, $\widetilde{\boldsymbol{Q}}$ and σ are the complex amplitudes and frequency, respectively; while $k_{x,z}$ are real wavenumbers. The dispersion relation $\sigma(k_x, k_z)$ and eigenvector are given in appendix D of LY17. We superimpose eigenvectors to obtain standing waves in z, as described by Youdin & Johansen (2007). We will refer to the dimensionless wavenumber $K_{x,z} \equiv k_{x,z}\eta_0 R_0$ and growth rate $S \equiv \mathrm{Im}\,\sigma/\Omega_{K0}$.

We carry out axisymmetric cylindrical (R, z) simulations. The domain is $[R_0 \pm 2\lambda_x, \pm\lambda_z/2]$, where $\lambda_{x,z} \equiv 2\pi/k_{x,z}$ is the SI wavelength. We apply periodic boundaries in z, but hold radial ghost zones at their initial values. In addition, we damp variables towards their initial values in the innermost and outermost 20 per cent of the radial domain on a time-scale of $t_\mathrm{damp} = 10^{-2}/s$, where s is the analytic SI growth rate. This treatment in radius is needed because we adopt radially global disc models, while analytic SI solutions

Table B1. Parameters for the streaming instability. Growth rates S are normalized by Ω_{K0}. The spread in measured growth rates across variables, ΔS_{sim}, is normalized by S_{sim}. The particle stopping time $\tau_{stop} = T_{stop}(1 + \epsilon_0)$.

Run	ρ_d/ρ_g	T_{stop} (τ_s)	K_x, K_z	Cells/λ	S	S_{sim}	ΔS_{sim}	Comment
A	3	0.025 (0.1)	30,30	64	0.4251	0.4437	0.5 per cent	Figs B1 and B2
B	2	0.0033 (0.01)	80,20	128	0.1203	0.1212	7 per cent	Fig. B3
C	3	0.001 (0.004)	160,40	128	0.1059	0.1134	12 per cent	Fig. B3

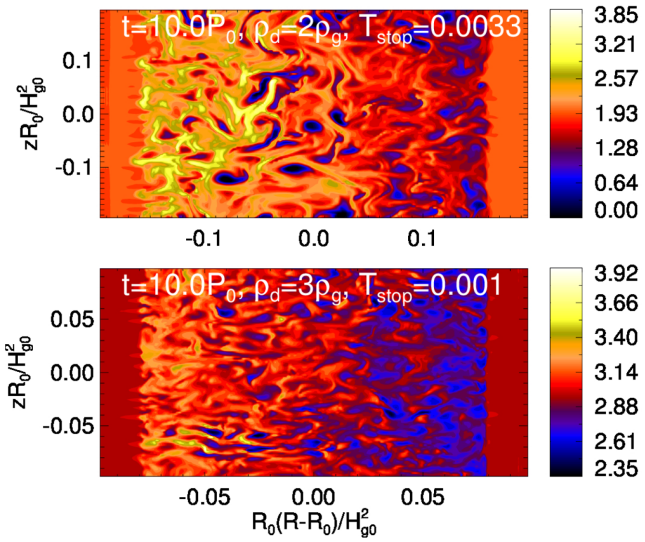

Figure B3. Dust-to-gas ratio at the saturated state of SI in run B with $\rho_d/\rho_g = 2$, $T_{stop} = 0.0033$ (top) and C with $\rho_d/\rho_g = 3$, $T_{stop} = 0.001$ (bottom).

assume periodicity in R. The extended radial domain with damping minimizes the influence of boundary conditions.

Since SI requires high accuracy, for this problem we configure PLUTO with piecewise parabolic reconstruction and third-order Runge–Kutta time integration. We use at least 64 cells per $\lambda_{x,z}$, corresponding to $>10^3$ cells per H_g. We impose a minimum dust-fraction $f_d > 10^{-6}$.

B3 Results

The simulations are summarized in Table B1. These are defined by the initial dust-to-gas ratio ϵ_0, stopping time T_{stop} or τ_{stop}, and the perturbation wavenumbers $K_{x,z}$. We also give analytic growth rates obtained from the one-fluid framework. We checked that these growth rates are nearly identical to that obtained from a full two-fluid analysis. We measure growth rates in the simulations by monitoring maximum deviations from equilibrium in $|R - R_0| < \lambda_x$ for each fluid variable. We report the mean value S_{sim}, and its spread across the variables, ΔS_{sim}. We find good agreement between simulations and the analytic growth rates.

Run A is same as the 'linA' code test used by other authors to benchmark their dusty-gas algorithms (Youdin & Johansen 2007; Balsara et al. 2009; Bai & Stone 2010; Miniati 2010; Yang & Johansen 2016). Fig. B1 shows exponential growth of hydrodynamic variables and Fig. B2 shows evolution of the dust-to-gas ratio. In the saturated state the dust-to-gas ratio ranges from zero to few 10s, showing strong particle clumping. This is consistent with previous numerical simulations with similar dust parameters (Johansen & Youdin 2007, their run 'AC').

Runs B and C adopt smaller T_{stop} and are shown in Fig. B3. We again find agreement with analytic growth rates in the linear phase, although the spread in S_{sim} increases with smaller T_{stop}. In the saturated state, Run B ($T_{stop} = 0.0033$) still develop voids with $\rho_d/\rho_g \sim 0$, but Run C ($T_{stop} = 0.001$) only develop order-unity fluctuations in ρ_d/ρ_g. Neither runs show strong particle clumping within the simulation time-scale. This is consistent with recent simulations of SI for small particles carried out by Yang et al. (2017). These authors find small particles only clump after integration time-scales $\gtrsim O(10^2)$ orbits.

APPENDIX C: DUST-SETTLING IN PROTOPLANETARY DISCS

We now consider vertically stratified discs. In the presence of vertical stellar gravity, dust settles towards the mid-plane of a protoplanetary disc on a time-scale of $t_{settle} \sim 1/\Omega^2 t_s$ (Takeuchi & Lin 2002). For $T_{stop} = 10^{-3}$ we expect $t_{settle} \simeq 160$ orbits. We demonstrate our hydrodynamic model of dusty gas reproduces this basic result.

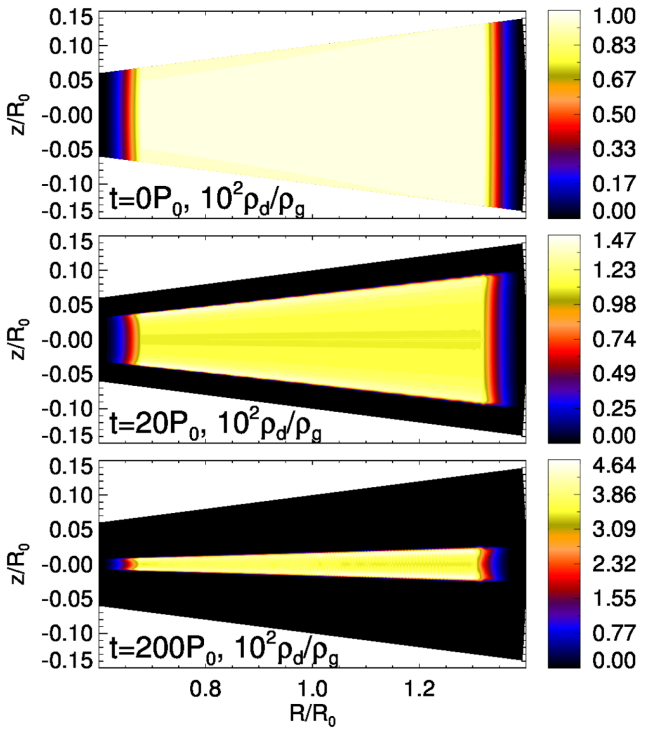

Figure C1. Dust-settling in a vertically stratified disc. The dust-to-gas ratio (scaled by 100) is shown. The reference stopping time is $T_{stop} = 10^{-3}$.

C1 Stratified disc model

We initialize the disc with an axisymmetric, steady state defined by

$$R\Omega^2 = R\Omega_{\rm K}^2\left(1-\frac{3}{2}\frac{z^2}{R^2}\right)+\frac{1}{\rho}\frac{\partial P}{\partial R}, \tag{C1}$$

$$0 = z\Omega_{\rm K}^2+\frac{1}{\rho}\frac{\partial P}{\partial z}. \tag{C2}$$

Given a dust-to-gas ratio distribution $\epsilon(R, z)$, we may solve equations (C1) and (C2) to obtain $\rho(R, z)$ and $\Omega(R, z)$. We use the thin-disc approximation for the star potential (equation13) in order to obtain analytic expressions below.

We set the initial dust-to-gas ratio to

$$\epsilon(R,z) = \epsilon_{\rm mid}(R)\times\exp\left(-\frac{z^2}{2H_\epsilon^2}\right). \tag{C3}$$

Here and below the subscript 'mid' indicates the mid-plane value, taken from the unstratified profiles described in Appendix B1. The characteristic thickness in the dust-to-gas ratio, H_ϵ, is defined via

$$\frac{1}{H_\epsilon^2}\equiv\frac{1}{H_{\rm d}^2}-\frac{1}{H_{\rm g}^2}, \tag{C4}$$

where the dust layer thickness $H_{\rm d}$ is parametrized by $\delta\equiv H_{\rm d}/H_{\rm g}<1$. As $\delta\to 1$ the dust becomes perfectly mixed with the gas, giving a vertically uniform dust-to-gas ratio.

Using equation (C3) we can integrate equation (C2) (taking the polytropic index $\xi = 1$) in z to obtain

$$\rho_{\rm g} = \rho_{\rm g,mid}\exp\left\{-\frac{z^2}{2H_{\rm g}^2}-\epsilon_{\rm mid}\frac{H_\epsilon^2}{H_{\rm g}^2}\left[1-\exp\left(-\frac{z^2}{2H_\epsilon^2}\right)\right]\right\}. \tag{C5}$$

The gas vertical structure is effectively Gaussian, since the z-dependence in the second term is weak (especially for well-mixed dust with $H_\epsilon\to\infty$). The total density is $\rho=\rho_{\rm g}(1+\epsilon)$ with ϵ given by equation (C3).

The disc orbital frequency is obtained from equation (C1),

$$\Omega(R,z)=\Omega_{\rm K}\left[1-\frac{3}{2}\frac{z^2}{R^2}+\frac{P}{\rho\,(R\Omega_{\rm K})^2}\left(\xi\frac{\partial\ln\rho_{\rm g}}{\partial\ln R}-q\right)\right]^{1/2}. \tag{C6}$$

Note that there is generally vertical shear, $\partial_z\Omega\neq 0$. This arises from a radial temperature gradient and/or a radial gradient in the dust-to-gas ratio (LY17).

By construction these initial conditions do not satisfy thermal equilibrium,

$$\frac{1}{R}\frac{\partial}{\partial R}\left(Rf_{\rm d}t_{\rm s}\frac{\partial P}{\partial R}\right)+\frac{\partial}{\partial z}\left(f_{\rm d}t_{\rm s}\frac{\partial P}{\partial z}\right)\neq 0.$$

However, since $\epsilon_{\rm mid}$ is chosen to minimize radial dust evolution (Appendix B1), this setup allows us to focus on vertical dust-settling.

C2 Simulations

For this problem we adopt an axisymmetric spherical grid (r, θ) with $r\in[0.6, 1.4]R_0$, $\tan(\pi/2-\theta)\in[-2, 2]h_{\rm g0}$, and $h_{\rm g0}=0.05$. We use a resolution of $N_r\times N_\theta = 840\times 240$, corresponding to about 50–60 cells per $H_{\rm g}$ at unit radius. We use logarithmic spacing in r but uniform spacing in θ. We return to linear reconstruction and second-order Runge–Kutta time integration, as used in the main text.

For the initial disc profile we use $p = 1$, $q\simeq -0.005$, and $H_{\rm d} = 0.99H_{\rm g}$ so the initial dust-to-gas ratio $\epsilon\simeq 0.01$ is nearly uniform both radially and vertically. We choose $|q|\sim 0$ to minimize vertical shear and associated instabilities (Nelson et al. 2013; Barker & Latter 2015; Lin & Youdin 2015), which would stir up particles and oppose dust-settling (Flock et al. 2017).

We taper ϵ to zero near radial boundaries in the initial setup, and apply reflective boundary conditions in both r and θ.

Fig. C1 shows the evolution of $\rho_{\rm g}/\rho_{\rm d}$. As expected the dust settles to a thin layer ($\sim 0.2H_{\rm g}$) on a time-scale of $\sim$100 orbits. Settling occurs outwards since more dynamical times have elapsed at smaller radii at a given snapshot. Notice early in the settling process the dust-to-gas ratio peaks near the surface of the dust layer. These results are similar to dust-settling simulations performed by Price & Laibe (2015).

This paper has been typeset from a TEX/LATEX file prepared by the author.